Invited Paper

Widely tunable CW QCLs THz sources at room temperature

M. Razeghi
Northwestern University, USA
* E-mail: razeghi@eecs.northwestern.edu

(Received December 30, 2018)

Abstract: The THz spectral region is of significant interest to the scientific community, but is one of the hardest regions to access with conventional technology. A wide range of compelling new applications are initiating a new revolution in THz technology, especially with regard to the development of compact and versatile devices for THz emission and detection. In this article, recent advances with regard to III-V semiconductor optoelectronics are explored with emphasis on how these advances will lead to the next generation of THz component technology.

Keywords: THz emitters, THz detectors, Semiconductor optoelectronics

doi: 10.11906/TST.093-154.2019.12.09

Introduction to THz radiation

A small portion of the electromagnetic spectrum, namely the terahertz (THz) spectral region in the frequency range 0.1-10 *THz*, corresponding to the energy range 0.4-41 *meV* or the wavelength range 3000-30 μm (see Fig. 1), is better known as the THz gap between the visible/infrared optoelectronics and the high frequency electronics. The non-availability of commercially viable THz radiation sources, detectors, and relevant components (e.g. lenses, mirrors, filters, coating, modulators etc.) shows that the technology of THz generation, manipulation and detection is still in its infancy. For the last two decades, tremendous efforts have been made by scientists in order to fill the THz gap. As a result, the rapid developments in the time-domain THz spectroscopy and related THz technologies including sources, components and detectors are becoming better in performance, and this will lead us to view the world in a completely new way.

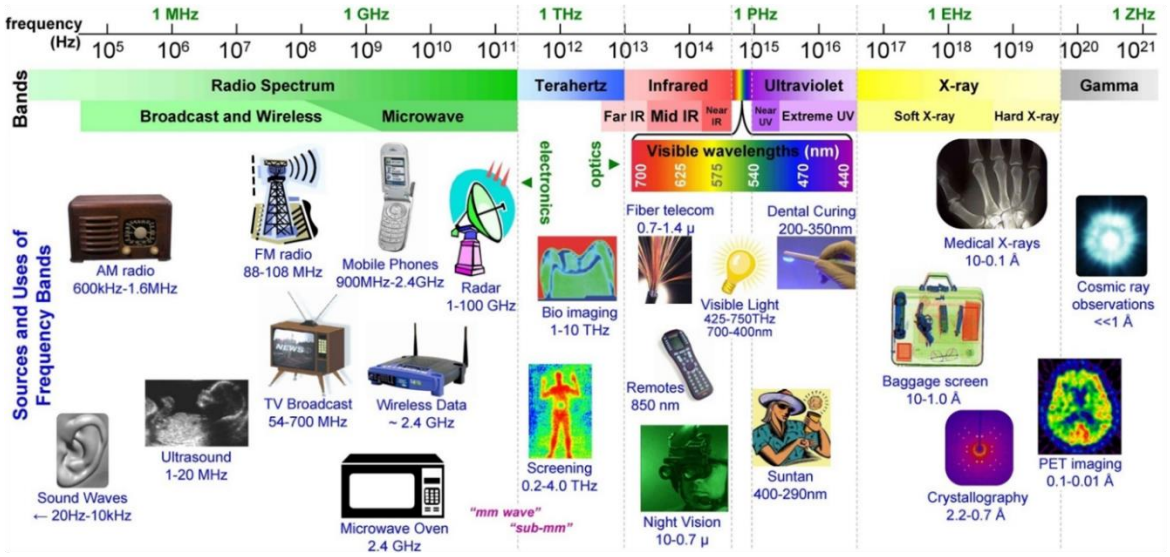

Fig. 1 Electromagnetic spectrum in frequency scale and typical applications. Adapted from Ref. [1].

THz regime is unique because of the very low energy of the radiation, which can penetrate through many materials whereas infrared/visible light will be blocked; also, being non-ionizing, it is non-destructive to biological tissues. But are THz waves completely safe? As the outreach of the opportunities for THz applications is profound, safety using THz radiation is worthy for investigation. A theoretical study by MIT in 2010 demonstrated that THz frequencies might interact with DNA through non-linear instabilities; however the process is probabilistic rather than deterministic [2]. Some available experimental data indicate that THz radiation has an influence on the biological functions, but only under particular conditions, like high power, and/or extended exposure, and/or specific THz frequency [3, 4, 5]. However, condensed matter is largely grouped into three types, namely, metal, water, and dielectric in regard to the optical properties at THz frequencies [6]. In this range, metals are highly reflective owing to the high electrical conductivity. On the contrary, water, a strongly polar liquid, can be highly absorbing in the THz region. Non-metallic and non-polar materials, i.e., dielectrics such as, plastic, ceramics, paper, clothes, woods, masonry etc. are transparent to THz radiation, whereas those are usually opaque at visible/infrared wavelengths.

To summarize, THz is our future. The advancement of THz technology is going to change the way we live and organize our world. In support, one can say that the bibliometric data indicates immense interest in terahertz science and technology. This is evidenced by the exponential rise of output in the scientific journal from the year 1975 [7].

Applications

THz regime is attractive for diverse applications in different fields and will be discussed briefly given the limited space in this review article.

Spectroscopy

The THz spectral range is remarkably valuable for spectroscopy, owing to the existence of rotational molecular bands that have absorption intensities akin to those of ro-vibrational transitions. Plenty of spectroscopy techniques like classical direct absorption spectroscopy or commonly used schemes, like wavelength modulation, differential spectroscopy, heterodyne spectroscopy, and quartz enhanced photoacoustic spectroscopy are possible and can be implemented.

Imaging

Quality control is one of the far reaching application types for the THz imaging technique. Since THz waves are strongly absorbed in water, they could be used to monitor the quality of food and agricultural products; for example, damaged fruits, vegetables can be identified and separated from the good ones. In industry, a final control (any defects like breakages, cracks, missing pieces etc.) of a packaged product without opening it could be done using the THz imaging. Specifically, in the semiconductor industry, fault analysis in the integrated circuits could be effectively detected using THz imaging technique. For example, normal MOSFET and damaged MOSFET made by focused ion beam could be separated via THz imaging [8]. THz tomographic imaging is now the routine inspection method to examine the foam insulation used for the space shuttle [9]. Reading antique books without touching, or reading a letter without opening the envelope could be possible using a real-time smart Terahertz imaging tool.

Medical and biological sciences

Since, THz waves can be strongly absorbed by the water molecules, and more than 70% of the human body is made of water, THz waves can distinguish cancerous tumors from healthy tissues. Therefore, for realizing a THz cancer diagnostic system, a lot of research is going on worldwide. Furthermore, development of THz endoscopy is necessary to widen the flexibility of the THz based diagnostic system to the internal organs of the human body. It is noteworthy that our goal at this time is to make pulsed THz power of ≥ 2.5 *mW* and CW power ≥ 0.1 *mW*, because this is sufficient for the THz endoscopy. Presently one example of useful THz endoscopy, is given by the photoconductive generator and detector driven by a mode locked Ti:sapphire femtosecond laser. This is done through dispersion compensated fibers based on the measurements of reflective THz signals from the side walls of the mouth, tongue, palm and skin, as reported by Ji *et al.* [10]. This system could be considerably miniaturized using on-chip THz generation based on THz DFG-QCLs eliminating completely the laser and its alignment parts and in this way decreasing the cost of the endoscopic system by a huge amount. Dental cavities detection is another important THz application.

Environmental monitoring

THz technology is having an important role in the environmental monitoring of our earth. Air temperature, humidity measurements, air turbulence studies, air pollution monitoring, hazardous gas detection and many more could be possible using this THz technology. Monitoring of atmospheric chemical species like OH, O_3, CO, HCl, HO_2, H_2O, HOCl, BrO, ClO, HNO_3, N_2O, HCN, CH_3CN, volcanic SO_2 etc. are possible using THz measurements [11]. To understand the ozone chemistry for global warming, NASA used a 2.5 *THz* laser to measure the concentration and distribution of the hydroxyl radical (-OH) in the stratosphere, a critical component in the ozone cycle. Another frequency line at ~3.5 *THz* is also important as it is near strong absorption signature of the hydroxyl (-OH) radical, whose change can be monitored for global warming. Hazardous gas detection could be used for saving lives and taking precautions on the spot; as an example, carbon monoxide gas detection at fire sites is possible where infrared gas detection is sometimes blocked, for example by concrete walls.

Security and defence

THz technology for security is expected to win over other technologies. The security application looks for hidden illicit smuggling materials like drugs, weapons like knives, guns, explosives etc. This kind of hidden materials detection is an important application field of THz. Because of the unique spectral fingerprints in the THz regime, different drugs (MDMA, aspirin, amphetamine etc.) and explosives (RDX, TNT etc.) can be easily recognized without touching the package.

Investigation on scattering of THz radiation by dielectric and conducting objects is of immense interest from the theoretical and experimental viewpoints. As the time-domain based THz systems could provide a fast precise and convenient method of revelation of scattering centers, it could be potentially used for military and defence related purposes like detection and recognition of ships, aircrafts and other targets plus countermeasures such as radar cross section (RCS) reduction and stealth [12, 13, 14, 15].

Astronomical studies and atmospheric sensing

THz range is important for astronomical research since 98% of the photons emitted since Big Bang is in sub-millimeter and far-infrared regime. Mostly, the THz photons are emitted by the dust and the gas between the stars, i.e., the interstellar medium (ISM) [16]. Hence we can have different kind of interesting information associated with the ISM of our own galaxy, the Milky Way, as well as from the ISMs of distant galaxies through these THz photons. Thus the outer space exploration will gain speed with the development of compact THz emitters and detectors, say the THz technology. A high resolution heterodyne spectrometer is needed driven by the demands of astronomical observations and atmospheric remote sensing in the THz frequency range.

Fundamental condensed matter research

Utilization of THz energy could be an important means for exploring the fundamental physics in different physical systems. Exploiting novel electronic and magnetic materials, characterizing superconductors, two-dimensional electron gas are a few examples. Many physical systems possessing characteristic energy values lie in the THz range like hybridization gap, Rydberg transitions, cyclotron resonance, phonons, excitons, collective excitations in spin materials etc. [17, 18, 19]. The physical phenomenon like Anderson localization can be observed in the THz range, which could be appealing for the development of random lasers [20]. Thus fundamental research in condensed matter could greatly benefit with the advancements made in THz technology.

Communications technology

It is known to all that the microwave frequencies are used for the present wireless communication system. However, because of the exponentially increasing data traffic, there is a huge demand of much faster data speed along with a larger bandwidth. Therefore, scientists believe that moving to the higher frequency range like THz is the promising one to cope up with such a huge demand. But why not directly turn to the near or mid infrared frequency range to put up wireless IR communication systems with several GB/s data rate? Presently it's not possible because of the poor receiver sensitivity and/or the limitation on the usage of high power not to cross the eye-safety limit [21]. Even though wireless IR systems are more than 40 years old, the highest data rates demonstrated so far are 155 *MB/s* [22, 23]. One journal publication concluded "The results prove that IR seems to be unable to replace RF for indoor LAN applications" [24]. Talking about the promising THz range, one drawback comes with the fact that the THz radiation is strongly absorbed in the earth's atmosphere. Consequently, the range of THz radiation propagation through the atmosphere is restricted to only tens/hundreds of meters, making it inappropriate and problematic for long distance communications. On the other hand, some basic estimation indicates that a line-of-sight connection between receiver and emitter is required in the THz communication systems unlike the present microwave based WLAN systems. The blocking of the direct line-of-sight connection could be avoided using non-line-of-sight paths which involve reflections off the walls. Dielectric mirrors mediated indirect transmission channels between a transmitter and receiver could ensure better signal coverage [21]. However, for indoor and short outdoor systems, THz wireless networking systems could be revolutionary.

Till date, GaAs and InP based integrated circuits are leading in all-electronic THz communications above 0.1 *THz*. However, other semiconductors based competing technologies are also running in the race to realize practical THz communications. One of them is the Si-based integrated circuit technologies (SiGe heterojunction bipolar transistors). For example, full demonstration of Si-CMOS based THz wireless link at 11 *GB/s* over a link distance of 3 meter was reported at a carrier frequency of 0.13 *THz* with real-time performance [25]. It is believed that the

combination of a compound semiconductor and Si based integrated circuits would accomplish the requirements of ultimate THz integrated circuits.

On the other hand, communication links enabled by THz photonics technologies could play a major part in realizing practical wireless THz system because of advantage of having very low loss optical fibers to input the THz emitting circuits, and control over multi-carrier, multi-format THz channels and switching carriers, which is unparalleled in electronics-based solutions [26]. A couple demonstrations of THz links based on photonics-based transmitters include a wireless data transmission of 32 *GB/s* with 16 quadrature amplitude modulation (QAM) over a link distance of 25 *meter* at a carrier frequency of 0.385 *THz* and a 50 *GB/s* real-time data transmission with OOK modulation over 100 *meter* at 0.33 *THz* [27, 28].

In spite of these impressive demonstrations, one of the present challenges to system functionality is the need for better transmitters and receivers with very high antenna gains and low-noise and wide-bandwidth THz amplifiers. Another challenge is to minimize the overall energy consumption without decreasing system efficiency. Scientists believe that photonic integration is the hopeful route to achieve the above. In practice, photonic integration is giving a boost to this technological progress, such as a single chip power transmitting of 0.1 *mW* at 0.1 *THz* with a total electrical input power of 1 *W*, including cooling, [27, 29] and integrating multiple photodiodes to realize a reasonable distance link service [28]. Furthermore, the advent of active Si photonics integration technology could potentially provide even better THz link efficiency from the perspectives of easier integration with matured mass-producible Si technology and Si based photonic waveguides with lower losses [30, 31].

Plasma diagnostics system

THz signals could be employed to understand the plasma turbulence behaviour in nuclear fusion reactors without much disturbing the delicate fusion material. There is an immense effort by a team of researchers in UK, China and USA to develop a compact, powerful and cost-effective THz vacuum electron device utilizing the latest micro-fabrication processes such that the traditional vacuum tubes can reach THz frequencies and subsequently monitoring the plasma behaviour.

In order to make such applications to be true, we need high power THz sources mainly at room temperature, sensitive THz detectors, and other functional devices. A historic breakthrough for science and technology accompanies with the advancement of the THz technology, which is built on many areas of science and diverse range of disciplines.

Existing sources

Electronic and photonic approaches are taken to extend their frontiers to bridge the THz gap. Some advantages and disadvantages are present in both the approaches to extend into the THz gap.

Electronic approach is a mature technology but suffers from the lower efficiency. Generally, it can provide <1 *THz*. On the other hand, photonics approach yields higher efficiency covering the THz range but it is multidisciplinary in fabrication from the material to the device. Specifically, THz sources are bulky, complex-operational, and cost-intensive, better suited for research laboratories over commercial usage. Realizations of on-chip, compact and mass producible THz sources will make this technology have a widespread social impact. THz sources can be organized as *pulsed* or *continuous* (as for the operation), narrowband or broadband (spectral coverage), *coherent* or *incoherent* (radiation properties) or the working principles. Sources generating THz (directly) via oscillation in electronic (solid state based or vacuum based) or in optical devices (e.g. lasers) are denoted as *direct*. On the other hand, sources generating THz via nonlinear mixing or conversion of electromagnetic pump waves in a nonlinear medium or in medium with accelerating electrons are called *indirect*. An overview of the available THz sources is given in Fig. 2. A summary of electronic THz sources is given in Tab. I, and a summary of optical THz sources is given in Tab. II.

Tab. I Summary of electronic THz sources.

	Room temperature?	**CW?**	**Frequency range**	**Power**	**Efficiency**	**Broad band or narrow band**	**Footprint**
Gunn diode	Yes	Yes	< 0.5 *THz*	*μW-mW*	10^{-5}-10^{-2}	Narrow band/ limited tunability	Chip size
IMPATT diode	Yes	Yes	< 0.4 *THz*	*μW-mW*	10^{-5}-10^{-2}	Narrow band/ limited tunability	Chip size
TUNNETT diode	Yes	Yes	< 0.4 *THz*	*μW-mW*	10^{-5}-10^{-2}	Narrow band/ limited tunability	Chip size
RTD	Yes	Yes	<1.1 *THz*	*μW-mW*	10^{-5}-10^{-2}	Narrow band/ limited tunability	Chip size
HMET	Yes	Yes	< 0.4 *THz*	*μW-mW*	10^{-5}-10^{-2}	Narrow band/ limited tunability	Chip size
HBT	Yes	Yes	< 0.4 *THz*	*μW-mW*	10^{-5}-10^{-2}	Narrow band/ limited tunability	Chip size
Frequency multipliers	Yes	Yes	< 3 *THz*	*nW-μW*	10^{-8}-10^{-5}	Narrow band/ limited tunability	Chip size
Gyrotron	Yes	Yes	< 1 *THz*	*W-MW*	-	Broad band	Room size
Free electron laser	Yes	Yes	Microwave to X-ray	*W-MW*	-	Narrow band/ wide tunability	Room size
Backward wave oscillator	Yes	Yes	< 1 *THz*	*mW-W*	< 50%	Broad band	Table top

Tab. II Summary of optical THz sources

	RT?	CW?	Frequency range	Power	Efficiency	Broad band or narrow band	Footprint
Photomixers	Yes	Yes	0.3- 3 *THz*	*μW-mW*	10^{-6}-10^{-3}	Narrow band/ wide tunability	Table top
Photoconductive switches	Yes	No	< 2 *THz*	*μW-mW*	10^{-6}-10^{-3}	Broad band	Table top
Parametric sources	Yes	Yes	0.3- 3 *THz*	*μW-mW*	10^{-6}-10^{-3}	Narrow band/ wide tunability	Table top
DFG in nonlinear crystals	Yes	Yes	0.3-3 *THz*	*μW-mW*	10^{-6}-10^{-3}	Narrow band/ wide tunability	Table top
Optically pumped FIR gas laser	Yes	Yes	0.3-10 *THz*	*mW-W*	10^{-5}-10^{-2}	Narrow band/ limited tunability	Table top

A highlighted overview of the available THz sources is presented below in Fig. 2 to comprehend in an elegant way with advantages and disadvantages.

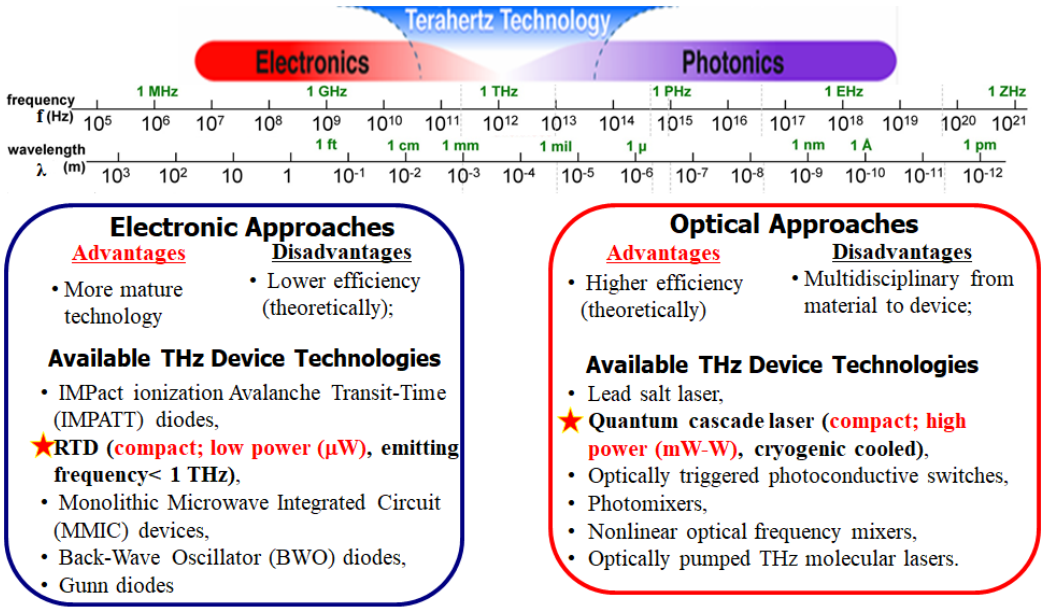

Fig. 2 Overview of available THz sources.

Semiconductor technology has revolutionized the world by providing compact and mass producible options for items such as the integrated circuit, which is the heart of computing, and the laser diode, which is the heart of telecommunications. Many of the technologies for THz generation are already based on semiconductor optoelectronics, with many more varieties currently in development. This review will now present current and future potential options in this area.

III-Nitride Material System for THz Optoelectronics

The III-Nitride material system (AlGaInN) is a versatile material system capable of being used to realize optoelectronic devices spanning the complete spectral range all the way from the deep ultraviolet (UV) to the terahertz. This material possesses a wide tunable direct bandgap, large longitudinal optical phonon energies, inherent fast carrier dynamics, good carrier transport properties, high breakdown fields, and high robustness and chemical stability. Thanks to these inherent advantages, III-Nitrides are being used to realize a wide array of optoelectronic devices including, lasers, photodetectors, and intersubband devices.

III-Nitride Material Growth

At the beginning of the III -Nitride boom of the 1990's there was a great rush to develop device quality material growth. The Center for Quantum Devices (CQD) at Northwestern University was among the first groups to realize high quality AlN on sapphire [32]. A key component of this work was development of a model for the AlN-Sapphire interface (Fig. 3) [33]. The CQD has demonstrated the capability to grow high quality AlGaN material across the compositional ranging from AlN to GaN.

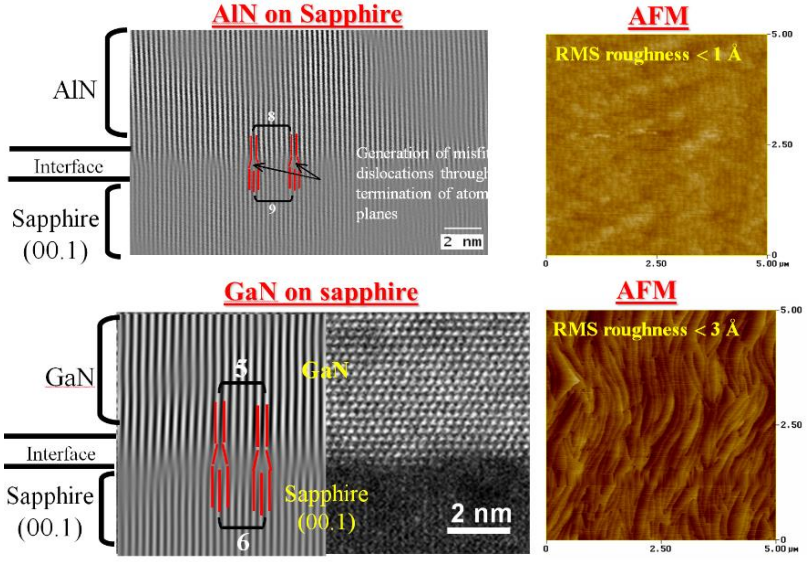

Fig. 3 Transmission electron microscopy (TEM) and atomic force microscopy (AFM) of Top) growth of AlN on sapphire and Bottom) growth of GaN on sapphire. Adapted from Ref. [33].

Ultraviolet Photodetectors and Focal Plane Arrays

AlInGaN is well suited to the realization of ultraviolet p-i-n photodiode UV detectors. The spectral response of a set of front illuminated $Al_xGa_{1-x}N$ p-i-n photodiodes with different Al compositions that we have realized is shown in Fig. 4. By tailoring the Al content in the active region from 0 to 70%, wavelength corresponding to the peak responsivity can be tuned from 364 to 232 *nm*. Due to the quality of the thick GaN templates, and careful device optimization, the

external quantum efficiency of these devices approaches the theoretical maximum for a p-i-n detector.

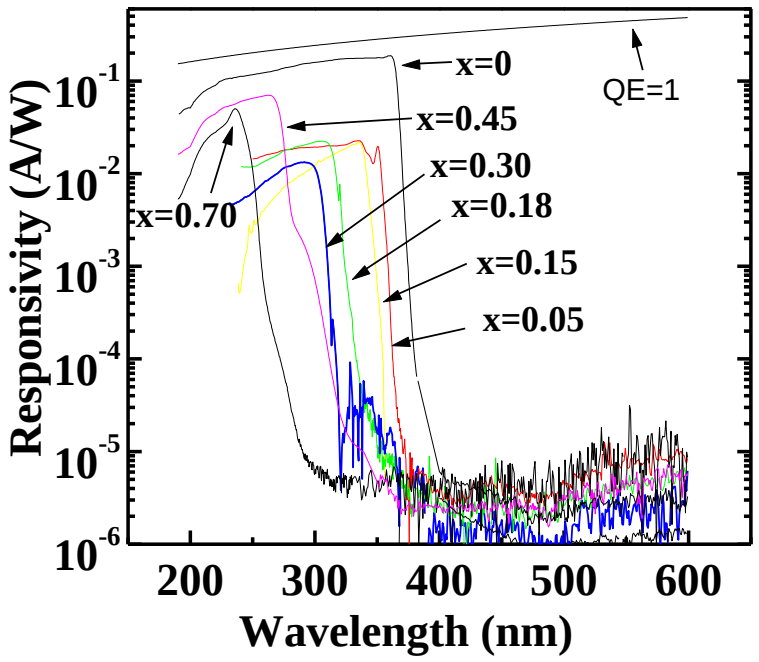

Fig. 4 The spectral response of a set of front illuminated $Al_xGa_{1-x}N$ p-i-n photodiodes with various Al compositions. The line at the top indicates the theoretical maximum for a p-i-n photodetector corresponding to a quantum efficiency of one. Adapted from Ref. [34].

Because of the low natural background in the solar-blind region (λ<290 *nm*), photodetectors and focal plane arrays (FPAs) operating in this spectral range allow for a number of unique applications [35]. These include covert space-to-space communications, secure non line-of-sight communications, early missile threat detection, hostile fire identification, ultraviolet (UV) spectroscopy, chemical and biological threat detection, UV astronomy, flame detection, power line and UV environmental monitoring [36, 37].

We have systematically optimized the device design and material doping through the growth and processing of multiple devices. This led the realization of a very high quantum efficiency of more than 89% from back-illuminated solar-blind (280 *nm*) photodetectors [38]. After optimization, uniform and solar-blind operation is observed throughout the array; at the peak detection wavelength of 275 *nm*, 729 μm^2 area PD showed unbiased peak external quantum efficiency and responsivity of ~80% and ~176 *mA/W*, respectively, increasing to 89% under 5 *V* of reverse bias (Fig. 5). Electrical measurements yielded a low-dark current density: $<2 \times 10^{-9}$ *A/cm*², at 10 *V* of reverse bias.

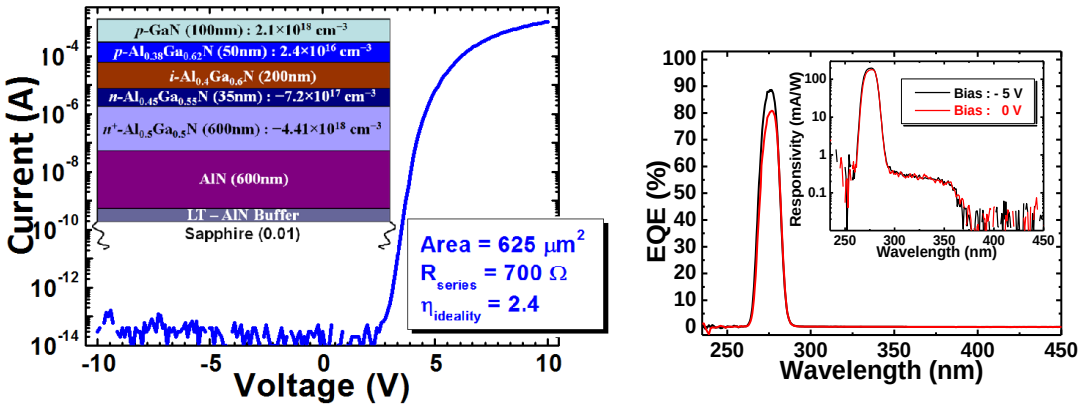

Fig. 5 LEFT) Very high quantum efficiency back-illuminated solar-blind photodetector device structure and current-voltage curve. RIGHT) external quantum efficiency of 89% under 5 V reverse bias. Adapted from Ref. [38].

Solar-Blind Focal Plane Arrays (FPAs). This same material can then be processed into an array of 256 x 320 pixels and hybridized to and Indigo Systems (FLIR) ISC9809 read-out integrated circuit (ROIC). A spatial mapping of the resulting quantum efficiency and peak detection wavelength for the array is shown below in Fig. 6 Left. The median external quantum efficiency of the array was 66% with a standard deviation of ±15%. The operability of this FPA was calculated as 92% (based on 2 standard deviations). Fig. 6(Right) below shows a solar-blind image from this FPA taken of a patterned aluminium plate illuminated with a UV arc lamp.

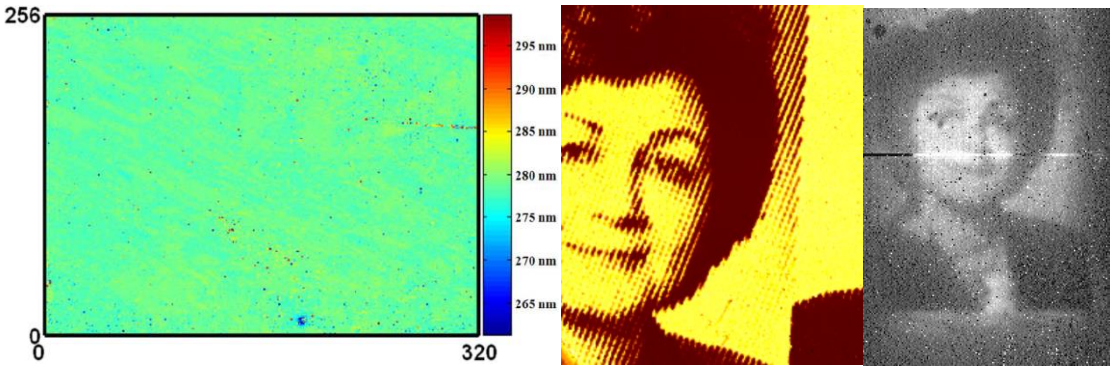

Fig. 6 Spatial map of the peak detection wavelength (LEFT) and a solar-blind ultraviolet image taken from the FPA (RIGHT). Because we did not have access to a UV lens, this image was taken by uniformly illuminating the FPA through a near-field shadow mask containing a dithered image of a face (MIDDLE). This new FPA represents a significant improvement over our first FPA (RIGHT) [39].

Avalanche Photodiodes (APDs). In order for solar- and visible- blind III-nitride based photodetectors to truly compete effectively with the detective performance of photo multiplier tubes (PMTs) there is a need to develop photodetectors that take advantage of low noise avalanche gain [35, 40, 41]. We were the first group to realize back illuminated GaN APDs on transparent AlN templates [42]. Using these structures, we have experimentally confirmed that hole-initiated multiplication provides superior performance in linear mode GaN APDs due to the higher hole ionization coefficient [43]. Back illumination results in higher gain and significantly reduced

excess multiplication noise performance (Fig. **7**). We have also developed a novel separate absorption and multiplication APD structure (SAM-APD) [44]. By separating the absorption and multiplication regions using a *p-i-n-i-n* structure it becomes possible to achieve nearly pure hole-injection, maximizing ionization coefficient resulting in a device with a maximum linear mode gain of nearly 80,000.

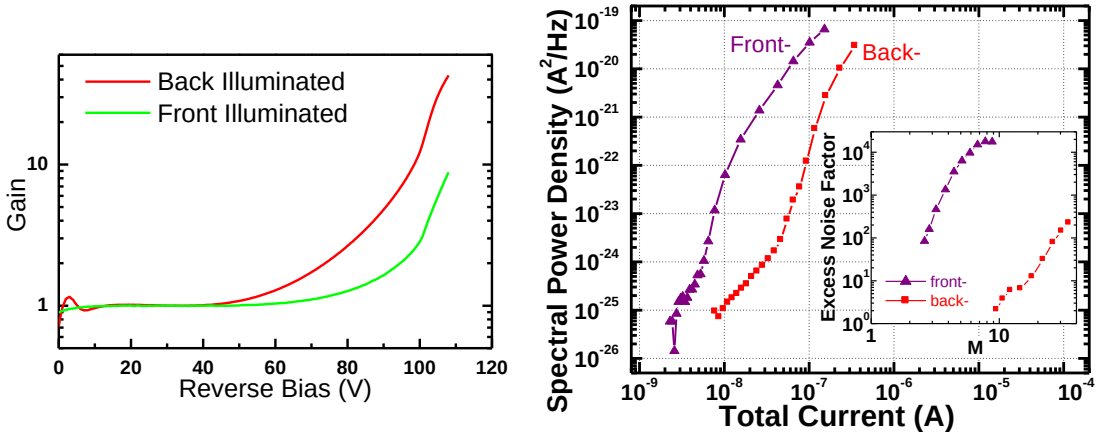

Fig. 7 Comparison of front- and back- illuminated perfromance of GaN APDs showing that back illumiation offer higher gain (left) and lower noise spectral power density and thus a lower excess noise factor (right). Adapted from Ref. [43].

Ultraviolet Emitters

There are numerous applications for ultraviolet light emitters: white LED for efficient-low-cost lighting, UV photolithography, high-density optical data storage, water purification, and portable chemical & biological agent detection/analysis systems are but a few.

Deep Ultraviolet Emitters. The quest for deep UV emitters started with the early effort in Japan to develop blue (~400 *nm*) LEDs and the first blue laser [45]. These devices can now be found in many systems, from cell phones to Blu-Ray players. They are also instrumental for white LED and laser projection systems currently being commercialized. However, blue lasers initially suffered from a very short lifetime (1 *sec*) in continuous operation [46]. Outside Japan, the first blue laser was demonstrated at CQD. Unlike Japan's first lasers, the CQD lasers did not exhibit any sign of degradation in continuous wave mode at room temperature, and were shown to be stable for a period longer than 160 *hours* [47, 48]. This demonstration helped instil confidence for further technological development in a now mature technology.

In order to achieve short wavelength emission, a high aluminium mole fraction is necessary, which makes the growth and doping of the material very difficult. Despite the problems associated with growth of high Al-content AlGaN films, the CQD has reported deep UV LEDs emitting at the critical wavelengths of 280 *nm*, 265 *nm*, and at wavelengths as short as 250 *nm* (Fig. 8).

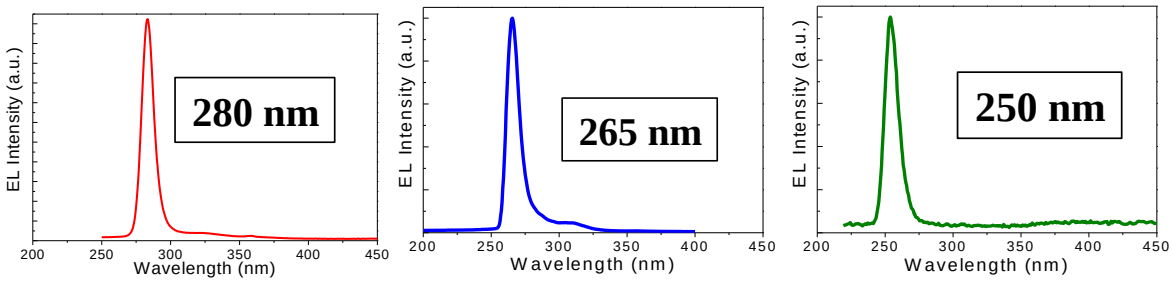

Fig. 8 Room temperature electroluminescence from deep-UV LEDs at 280 nm, 265 nm, and 250 nm. Adapted from Refs. [49, 50].

For the 280 *nm* devices, the dominant electroluminescence peak occurs at 280 *nm*, with a FWHM of ~10 *nm*. The pulsed power (200 *ns* pulses, at 200 *Hz*) of an array of four 300 μm × 300 μm devices reaches 5.6 *mW* [49]. Similarly, the CQD was the first group to report deep UV LEDs at the critical wavelengths of 265 *nm* and 250 *nm*, with powers of 5.3 *mW* and 2.7 *mW*, respectively [50].

Surface Plasmon Enhanced UV LEDs. Among the many recent approaches leading to improved quantum efficiency in UV LEDs devices, surface plasmons (SPs) have been actively studied. SPs are the collective oscillations of free electrons at a metal-dielectric interface. Because of the increased photon density of states near the SP frequency, QW-SP coupling provides a fast path for electron-hole recombination and increases the spontaneous emission rate.

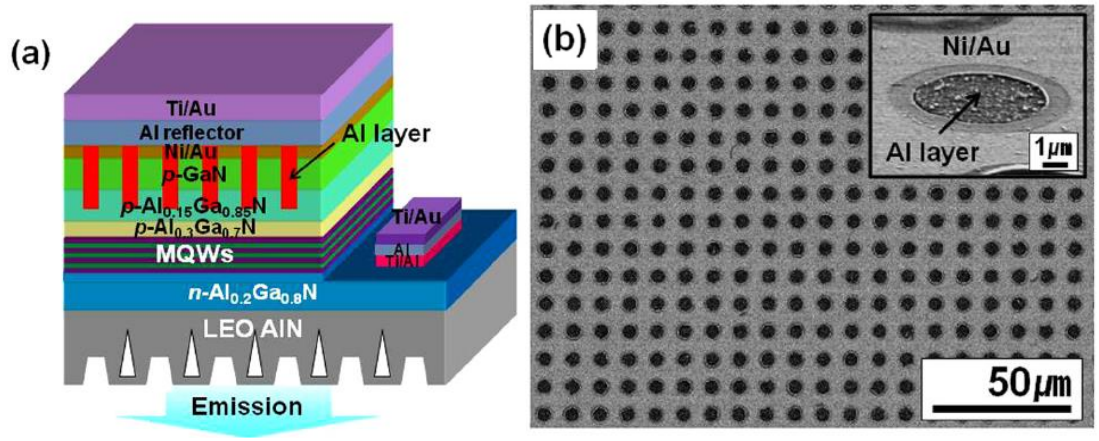

Fig. 9 (a) Schematic diagram of a back-emission surface plasmon enhanced UV LED grown on silicon. (b) Scanning electron micrograph (SEM) of the aluminium surface plasmon layer deposited on the top of the UV LEDs. Adapted from Ref. [51].

An aluminium layer was selectively deposited close to the MQWs such that the induced near fields around the aluminium layer could strongly interact with the QW (Fig. 9). At 700 *mA*, the SP-enhanced UV LED with an Al layer showed 45% higher light output than a conventional UV LED without an Al layer allowing a peak pulsed power of 1.2 *mW* to be achieved. The large enhancement of optical output power is attributed to improvement of internal quantum efficiency in MQWs resulting from increased spontaneous emission rate by the QW-SP coupling [51].

Blue-violet laser diodes. The short wavelength blue-violet laser is of immense importance in order to use for the optical data storage likely in compact disk, digital video disk, imaging industry etc. We had previously demonstrated excellent results on 405 *nm* blue-violet laser diode comprising of InGaN/GaN multi-quantum wells [52].

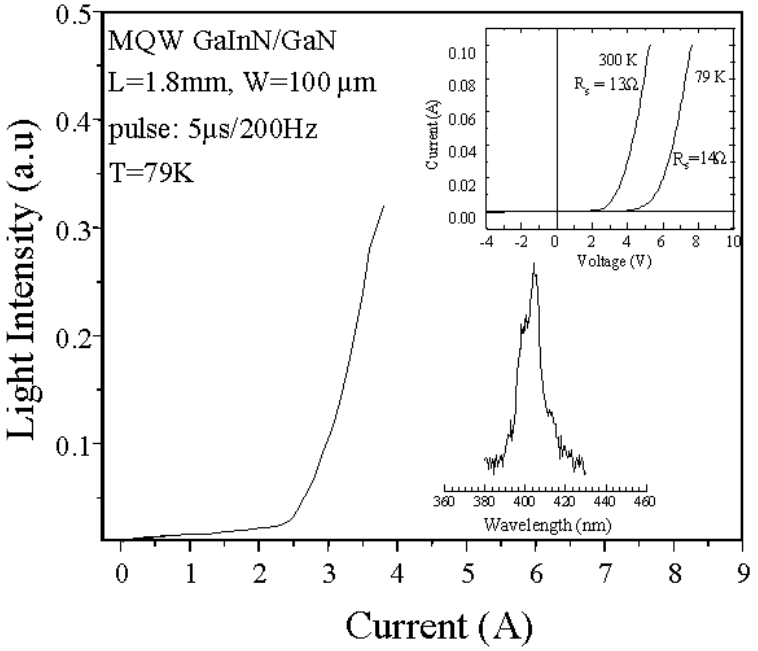

Fig. 10 Output power as a function of injection current for a 405 *nm* diode laser. Upper inset: current–voltage characteristics of the laser diode with series resistance of 13 *Ohm* at 300 *K* and 14 *Ohm* at 79 *K*. Lower inset: emission spectrum of the laser diode slightly above the threshold. Adapted from Ref. [52].

The device structure consisted of a 10-period 6.6 *nm* GaN/3.3 *nm* $Ga_{0.89}In_{0.11}N$ multi-quantum well active region grown on top of a 3 *μm* thick n-GaN and capped by 250 *nm* of p-GaN using basal plane sapphire substrate. Laser bar with a 1.8 *mm* cavity length showed threshold current density of 1.4 kA/cm^2 at 79 *K*, which is a low value considering the high dislocation density in the epilayers. The peak wavelength of the lasing is 405 *nm* at 3.4 *A* as shown in the Fig. 10. No degradation was observed below 4 A current under pulsed operation.

UV Photodetectors & Emitters on Silicon Substrates.

Conventionally, III-Nitrides are grown on Sapphire substrates. However, silicon is a significantly lower cost substrate available in larger wafers. The realization of back-emission/detection UV devices on silicon is challenging because silicon is UV opaque, and because of the large lattice/thermal expansion mismatch between AlGaN and silicon. We have developed a novel pattering to reduce the strain and cracking (Fig. 11).

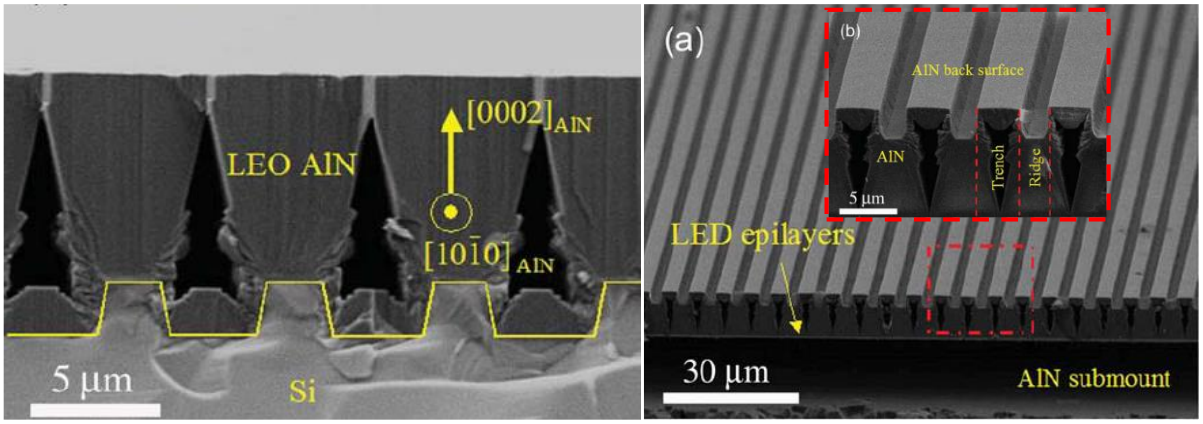

Fig. 11 RIGHT) Regrowth of AlN on pattered silicon substrates results in a smooth coalesced surface. LEFT) After flip-chip bonding the device, the substrate can then be selectively removed via wet etching. Adapted from Ref. [54].

Both back-illuminated photodetectors and back-emitting light emitting diodes (LEDs) have been realized on silicon substrates using this technique [51, 53, 54]. Photodetectors with an area of 625 μm^2 achieved, at the peak detection wavelength of 290 *nm*, an unbiased peak external quantum efficiency of 7% and a responsivity of 18.3 *mA/W*. The UV and visible rejection ratio was more than three orders of magnitude. Electrical measurements yielded a low-dark current density below 1.6×10^8 A/cm^2 at 10 *V* reverse bias [53]. A peak pulsed power and slope efficiency of 0.6 *mW* and 1.3 $\mu W/mA$ were observed from these thin-film UV LEDs, respectively; for comparison, top-emission UV LEDs were fabricated and observed to have 50% lower efficiency [54].

Terahertz Intersubband Devices

The terahertz spectral range offers promising applications for science (such as cancer detection), industry (such as product defect detection), and military (such as drug, concealed weapon or explosives detection), and III-Nitrides are theoretically capable of THz lasing at room temperature (RT). Recently, AlN/GaN and AlGaN/GaN superlattices are employed to show intersubband absorption in near- and mid-infrared spectra, respectively (Fig. 12-Left). Moreover, $Al_xGa_{1-x}N$/GaN resonant tunnelling diodes have been shown to possess negative differential resistance at RT. These recent demonstrations motivate THz emitters based on GaN at RT. The effects of lattice-mismatched (sapphire) versus lattice-matched (GaN) substrates and polar (c-plane) versus non-polar (m-plane) substrates on detectors and intersubband devices have been studied [55]. The emerging low-dislocation free standing substrates have shown promise for resonant tunnelling diodes (Fig. 12-Right) [56].

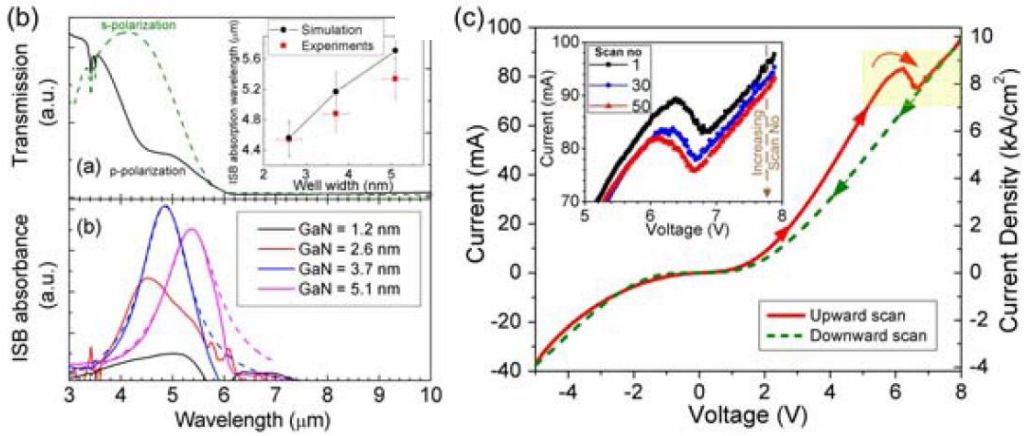

Fig. 12 Inter- and intersubband III-nitride devices: (LEFT) Demonstration of intersubband absorption and its dependence on GaN well width in mid-infrared. Inset compares the theoretical calculations with experimental results. (RIGHT) Demonstration of first resonant tunnelling quantum device with reliable negative differential resistance in GaN material system. The inset shows the stability of the negative resistance over fifty measurements. Adapted from Ref. [56].

Comparison of a narrow bandgap material with a III-Nitride material with respect to the optical phonon energy is shown through band diagram (Fig. 13), which elucidates the superiority of the later one in regard to the temperature sensitivity.

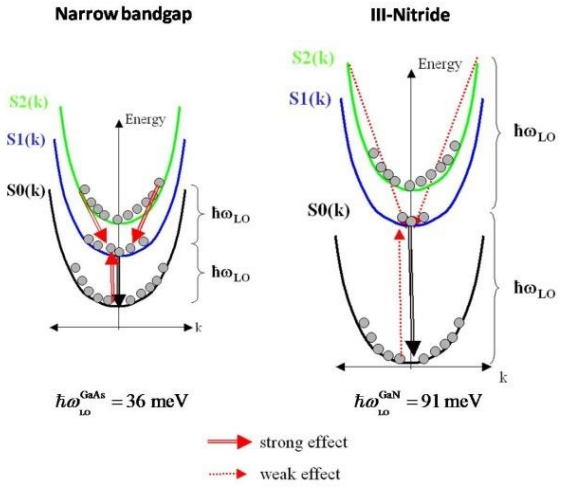

Fig. 13 Schematic diagram of a narrow bandgap and III-Nitride material intersubband levels in regard to the optical LO phonon energy

The optical phonon energy, $\hbar\omega_{LO}$, in narrow bandgap semiconductors is typically 30-40 *meV*. Thermal excitation from S0 to S1 reduces the population inversion. At 300 *K*, 25 to 30% of the ground state (S0) electrons may be found in S1. At low temperatures, as long as (S2-S1)<$\hbar\omega_{LO}$, the electron lifetime at S2 is sufficiently long to have a good population inversion. At higher temperatures, electrons with higher kinetic energy on S2 have enough total energy to emit an optical phonon and relax directly to S1. This non-radiative transition significantly decreases the

optical gain. III-Nitride material will significantly improve this situation because of the substantial lessening of the thermal backfilling owing to the higher phonon energy (91 *meV* for GaN). Thus III-Nitride material could be a promising candidate for the room temperature or thermoelectrically cooled THz quantum cascade laser.

GaAs-Based Devices for THz Optoelectronics

High Power and High Efficiency GaAs-Based Lasers

Most early devices on GaAs substrates were built from GaAs/$Al_xGa_{1-x}As$ heterostructures. While adding Al significantly changes the band gap of the material, the lattice constant changes slowly across the entire Al compositional range. This makes it easy to engineer novel band structure for electrical and/or optical confinement. However, it was found early on that incorporating Al introduces other problems for devices including: oxygen incorporation, deep level traps, the formation of dark line defects, rapid oxidation in atmosphere, catastrophic optical damage, and rapid degradation. While not a serious problem for low power, inexpensive devices, these issues have a very high impact on high power devices, especially laser diodes used for pumping fiber amplifiers and solid state laser crystals.

In order to circumvent these problems, another compatible, yet versatile, material system was developed as a replacement for AlGaAs. The $Ga_xIn_{1-x}As_yP_{1-y}$ system can also be lattice-matched to GaAs and has a wide wavelength range from 630–870 *nm*. The major hurdle is the optimization of the material quality, which requires strict composition control through careful control of growth procedure.

The validation of this material system began with the invention of high quality GaAs/$Ga_{0.49}In_{0.51}P$ heterojunctions, multi-quantum wells, and superlattices by metalorganic chemical vapour deposition (MOCVD) [57]. These heterojunctions boasted Hall mobilities up to 8000 $cm^2/V\text{-}s$ at 300 *K* and 800,000 $cm^2/V\text{-}s$ at 2 *K* [58], followed by the discovery of the first two-dimensional electron gas (2DEG) in the same system [59]. This discovery in particular is very important for any device requiring abrupt interfaces.

Further improvements in material quality and compositional control led to high performance Al-free laser diodes along with related patents [60, 61]. Optimized 808 *nm* laser diodes based on GaAs/GaInAsP with uncoated facets emitted high output powers of 10 *W* and 7 *W* in pulse and continuous wave operation, respectively. Laser bars yielded output powers of 70 *W* in quasi-continuous wave operation [62, 63]. Both of these were significant accomplishments at the time. Using this alternative material system, the catastrophic optical damage threshold was extended to >6 MW/cm^2 for uncoated facets, which was 5-10 *times* higher than that achieved with Al-based

lasers. At the same time, these high quality GaInAsP laser structures were capable of producing a narrow transverse beam with a divergence of only 26°, significantly narrower than the 32-48° values for commercial AlGaAs lasers at the time.

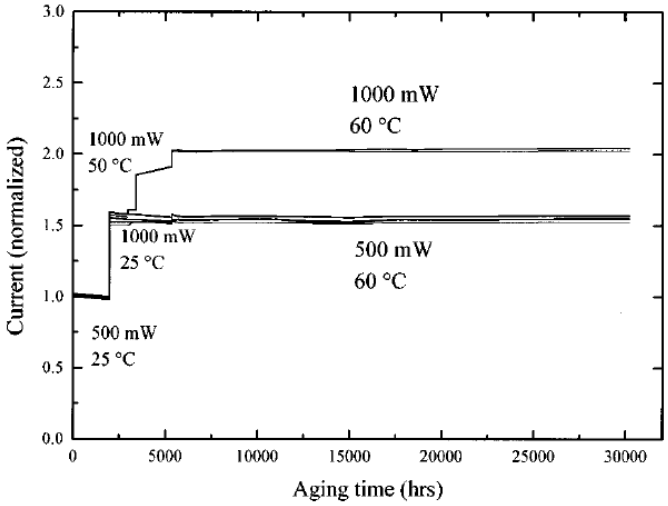

Fig. 14 Reliability testing data for Al-free near-infrared diode lasers fabricated at CQD. Reprinted from Ref. [65, 66].

Another important advance in this material system was the realization of high performance semiconductor lasers emitting at 980 *nm* through the use of strained InGaAs quantum wells inside a separate confinement heterostructure (SCH), which was also Al-free [64]. The longer wavelength emission is important for pumping fiber amplifiers used in telecommunications. These MOCVD-grown lasers exhibited both a low threshold current density and a high output power. A key achievement at the time was achieving a low waveguide loss which led to an external quantum efficiency of 75%. A very high characteristic temperature T_o of 350 *K* was also demonstrated, which was very favorable compared to the value of 160 *K* for Al-containing lasers at the time. Another highlight of the 808 and 980 *nm* lasers is improved durability. Even while testing in continuous wave at 1 *W* and 60 ℃, they exhibited no degradation over 30,000 *hours* (Fig. 14) [65, 66].

The combination of high power, efficiency, and reliability were key selling points for the Al-free laser technology described above. This technology was patented and licensed from Northwestern University for production in 1997, and variations on the original structures are still in production today [67]. High power pump laser bars are now standard components in industrial and government systems, and research is focusing now on small improvements in efficiency and thermal packaging.

GaAs-Based Intersubband Photodetectors

Intersubband transitions can also be engineered in this material system to absorb or emit photons in the mid-infrared or THz region. One example of such a device is the quantum well infrared

photodetector (QWIP), which is based on intersubband absorption within a conduction band quantum well. Though most initial research was based on GaAs/AlGaAs heterostructures, alternative QWIP designs based on Al-free heterostructures were also developed. This was done to benefit from the lower surface recombination velocity, improved electrical properties, and easier processing requirements, similar to the arguments that led to development of Al-free near-infrared lasers.

In 1995, the first Al-free p-type GaAs/GaInP QWIP using a Low Pressure MOCVD reactor was successfully demonstrated [68]. These p-type detectors showed normal incidence detection and were analyzed in some detail using a model based on an eight band Kane Hamiltonian [69]. LWIR n-type QWIPs were then developed based on GaAs/GaInP which exhibited low dark current and high gain [70].

Despite the material improvements that were demonstrated with QWIP technology, there are inherent drawbacks due to one dimensional carrier confinement that make it difficult for QWIPs to achieve high performance at higher operating temperature. Utilizing 3-D carrier confinement instead, the quantum dot infrared photodetector (QDIP) has emerged as a potential candidate for the next generation of IR imaging technology. 3-D carrier confinement provides the QDIP many advantages over the traditional QWIP, such as sensitivity to normally incident radiation. Quantum dots are also predicted to show higher gain and less temperature sensitivity due to suppressed longitudinal optical (LO) phonon interaction. The QDIP is also expected to exhibit lower dark current than HgCdTe detectors and QWIPs due to 3-D quantum confinement of the carriers inside the potential well. To allow for more versatile tailoring of absorption and carrier transport, a hybrid design called the quantum dot-in-well infrared photodetector (QDWIP) is also utilized which combines advantages of both quantum dot and quantum well detectors.

Some of the first QDIP devices were based on InGaAs/GaAs/GaInP heterostructures grown on GaAs substrates [71]. These devices were designed to absorb at a wavelength near 5 μm, and were operated near 77 K. By 2004, the first 256×256 FPAs based on QDIPs was demonstrated [72].

GaAs-Based Quantum Cascade Lasers

THz quantum cascade lasers (QCLs) have been most commonly realized using the GaAs/$Al_xGa_{1-x}As$ material system, for which lattice matching can be obtained over a wide range of barrier compositions, allowing the adjustment of the barrier height [73]. However, $Al_xGa_{1-x}As$ has major drawbacks, such as high reactivity with oxygen, and donor-related deep traps (DX centres) [74]. Alternative candidates with lower effective electron mass include InGaAs/ InAl(Ga)As, InGaAs/GaAsSb, and InAs/AlAsSb with compositions lattice matched to InP or InAs, respectively [75, 76, 77, 78]. The latter is very promising due to the lowest effective mass; however only lasing in magnetic fields has been achieved so far. A more mature choice is the InGaAs/InAlAs material combination, which is well developed and already commonly used for

mid-infrared QCL devices [79, 80]. However, this material involving Al components has a strong interface roughness scattering mechanism which hampers the laser's high temperature performance [81].

On the other hand, the GaAs/ $Ga_{1-x}In_xP$ lattice-matched material system represents a new attractive option for THz QCLs [57, 82]. Without using Al, the issue of interface roughness of these material is greatly relieved compared with other material system. The low-temperature mobility of the electrons at this interface has been reported to be of 800,000 $cm^2V^{-1}s^{-1}$ for a sheet carrier density of 3.5×10^{11} cm^{-3} which is much higher than other material system [83]. The conduction band offset ranging from 200 to 390 *meV* is perfect for quantum design of THz QCL active region [84].

Sb-containing Devices for THz Optoelectronics

The MOCVD growth of InSb, InAsSb, InSbBi, InAsSbBi, InTlSb and InTlAsSb materials and corresponding use for the detection purposes extending the applications of these materials to the end of the mid infrared region had been experimentally investigated by Prof. Razeghi's group. Due to the very low bandgap of these materials, it helps us to consider for the probable use for the THz optoelectronics via further band gap engineering in near future. In the next few sections we will shortly discuss about the performance of the above said materials.

InSb-Based Devices

Successful growth of high quality InSb on GaAs, Si, and Al_2O_3 substrates had been accomplished by MOCVD and MBE [85, 86, 87, 88, 89]. For InSb on GaAs substrate, X-ray linewidth was as low as 55 arcsec for a 10 μm epilayer, peak mobilities as high as ~125,000 cm^2/V-*s*, and carrier lifetimes up to 240 *ns* at 80 *K*. We had demonstrated first time the InSb photoconductors on GaAs substrate, showing the maximum voltage responsivity of 1000 *V/W* at 77 *K*. The corresponding figures are shown below. This is the world's first demonstration of InSb photoconductor with such a high responsivity. Not only the single pixel format of InSb detector, but also focal planar arrays out of it were demonstrated.

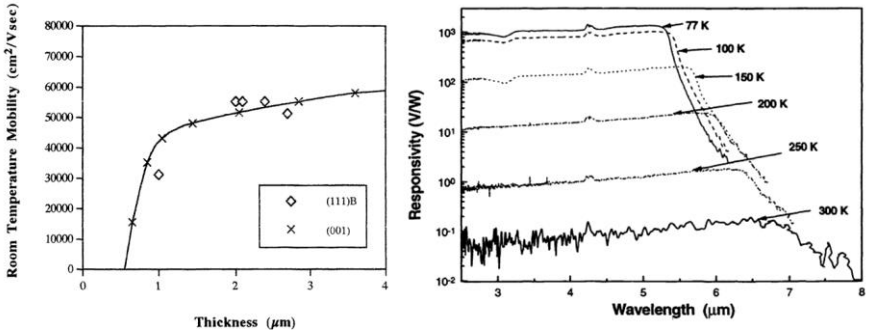

Fig. 15 (a) Mobility vs. thickness of InSb epilayer grown on (100) and (111) GaAs. (b) Spectral response of an InSb photoconductor on (111) GaAs for different temperatures. Adapted from Ref. [89].

InAsSb-Based Devices

For this kind of material (As was included along with Sb), the photovoltaic and photoconductive devices were grown successfully on GaAs and Si substrates using MBE[90, 91, 92, 93]. X-ray FHWM was ~300 arcsec (5 μm thick) indicating the excellent epitaxial character. At 300 *K*, the photovoltaic detectors on GaAs substrates exhibited a sharp cut-off wavelength of 7.5 μm with a peak responsivity of 0.32 *V/W* at 6.5 μm (see Fig. 16). The Johnson noise limited detectivity was estimated to be 4.2×10^7 Jones at 300 *K*.

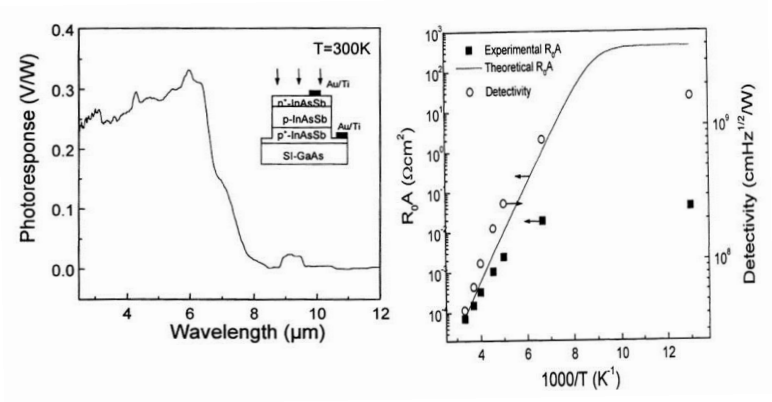

Fig. 16 (a) Voltage responsivity vs. wavelength for an InAsSb based photovoltaic detector (b) Detector resistance and area product along with the detectivity as a function of inverse temperature. Adapted from Ref. [93].

To extend the cutoff wavelength compared to the previous one, we have implemented a device structure based on p-$InAs_{1-x}Sb_x$/p-InSb heterostructures grown on GaAs substrates by MOCVD. Photoresponse up to 14 μm has been obtained in a sample with x=0.77 at 300 *K* (see Fig. 17(a)). The Johnson noise limited detectivity at λ=10.6 μm is estimated to be about 3.27×10^7 *cm* $Hz^{½}/W$ at 300 *K*.

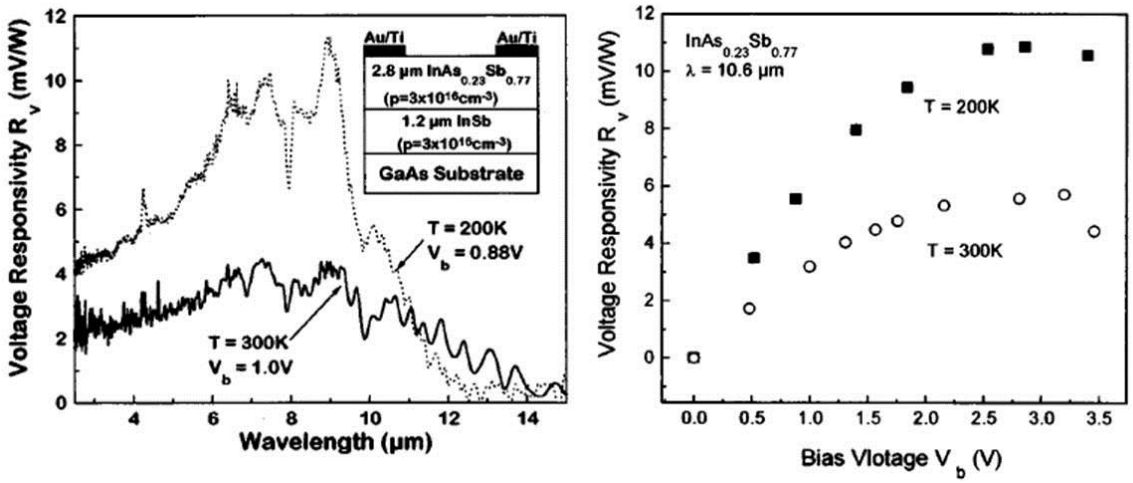

Fig. 17 (a) Photoresponse spectra of p-$InAs_{1-x}Sb_x$/p-InSb based device on GaAsat 200 *K* and 300 *K* (b) Bias dependent voltage responsivity at 10.6 μm for 200 *K* and 300 *K*. Adapted from Ref. [91].

Thus the implementation of InAsSb Alloys on GaAs and Si Substrates in order to achieve uncooled infrared photodetector applications for 5–8 μm or even longer range was successfully executed as a world's first demonstration.Another important demonstration was based on InAsSb/AlInSb double heterostructure detectors for room temperature operation, which exhibited a cutoff wavelength at 8 μm at 300 K, a high quantum efficiency of 40%, a responsivity of 0.3 A/W at 7 μm under a reverse bias of 0.25 V and a Johnson noise limited detectivity of 2×10^8 $cmHz^{1/2}/W$.

InSbBi-Based Devices

Bismuth (Bi) is another group-V material, which was successfully incorporated along with Sb as $InSb_{1-x}Bi_x$ epilayers on InSb and GaAs by LP-MOCVD growth [94, 95, 96, 97]. Photoresponse of InSbBi epilayers showed the cut-off wavelength up to 9 μm at 77 K. Cut-off wavelengths are highly sensitive to the Bi content; with increase in Bi content, cut-off is red-shifted. Spectral photoresponse for different x-values is shown in the Fig. 18.

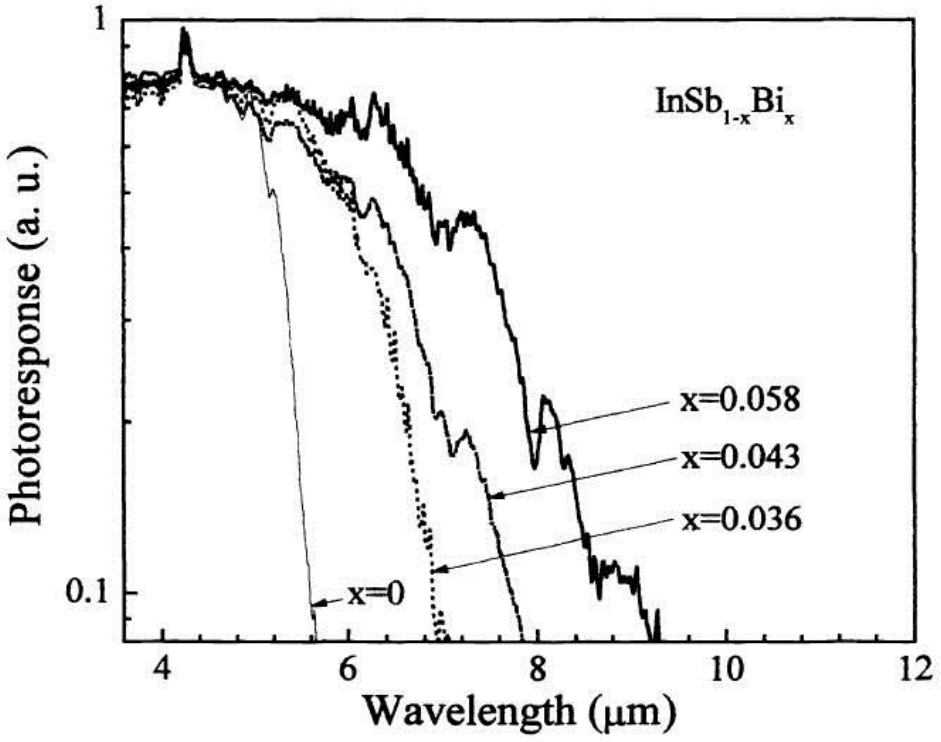

Fig. 18 Normalized photoresponse of $InSb_{1-x}Bi_x$ photoconductors for various compositions at 77 K. Adapted from Ref. [94].

Operation of InSbBi based photoconductors up to 200 K could be observed with the cutoff wavelength extended up to 9 μm (for $InSb_{0.96}Bi_{0.04}$), as shown in the Fig. 19(a). Bias dependency is observed too (see Fig. 19(b)).

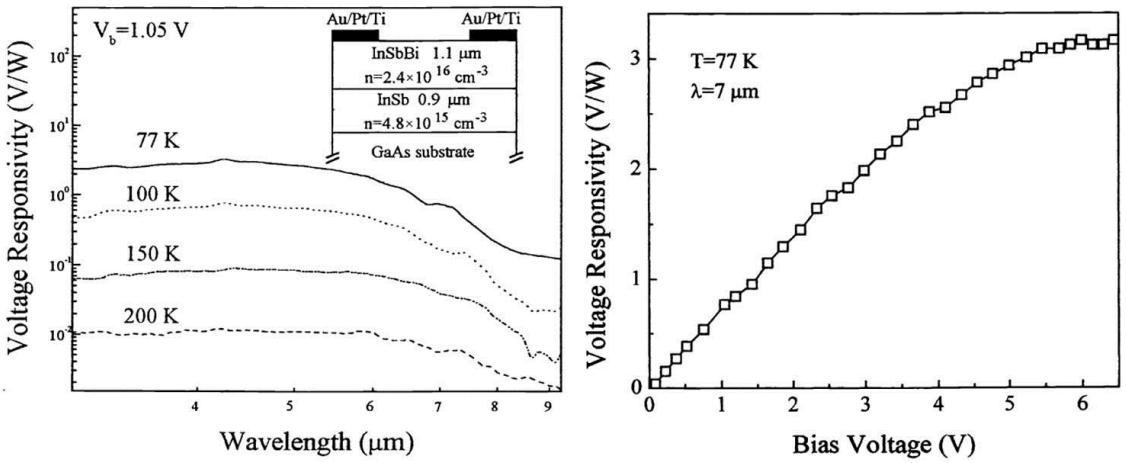

Fig. 19 Voltage responsivity of $InSb_{0.96}Bi_{0.04}$ photoconductors as a function of (a) wavelength and (b) bias voltage. Adapted from Ref. [97].

Room temperature operation out of InSbBi photoconductor could be also accomplished using $InSb_{0.95}Bi_{0.05}$ on GaAs substrate; this being the world's first demonstration with photo-response up to 12 *μm* at room temperature, with a peak responsivity of 4.7 *mV/W* (see Fig. 20). Another world first demonstration was about 6.6 *V/W* responsivity at 77 *K*, corresponding to a Johnson noise limited detectivity of 4.7×10^8 $cm.Hz^{0.5}/W$.

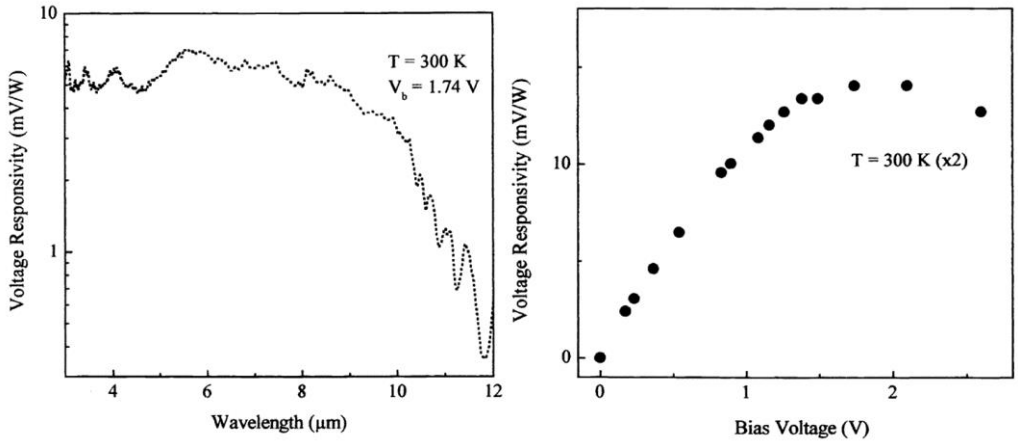

Fig. 20 Room temperature voltage responsivity of $InSb_{0.95}Bi_{0.05}$ photoconductors as a function of (a) wavelength and (b) bias voltage. Adapted from Ref. [95].

InTlSb-Based Devices

World's first successful growth of Thallium (Tl) based (InTlSb) epilayer by LP-MOCVD was accomplished in CQD [98, 99, 100, 101, 102]. The bandgap could be engineered to 110 *meV* (at 300 *K*). X-ray diffraction pattern exhibited FWHM of ~3,000 arcsec for a 2 *μm* thick film. Previously, the cut-off wavelength of only InSb had been observed 5.5 *μm* at 77 *K*. As Tl was incorporated, cut-off wavelengths of $In_{1-x}Tl_xSb$ shifted to longer wavelength and it is a monotonic

increasing function with increasing Tl composition. Cut-off wavelength at 77 *K* is 9.5 *μm* for x=0.06, as shown in the Fig. 21. Not only restricted to the liquid nitrogen temperature, but also the room temperature demonstration of world's first uncooled InTlSb photodetectors was successfully executed. Response up to 11 *μm* at room temperature from $In_{0.96}Tl_{0.04}Sb$ layers had been obtained and presented below in the Fig. 21 (right panel).

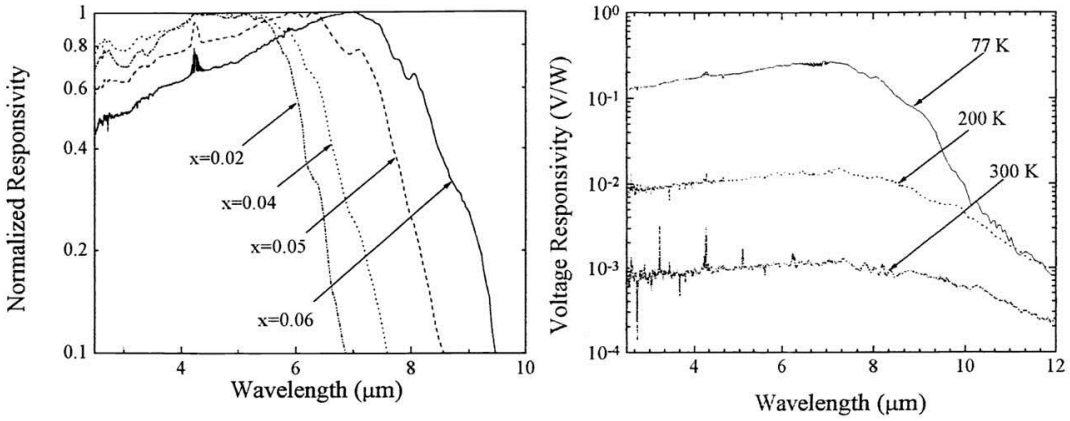

Fig. 21 (a) Normalized photo-response of $In_{1-x}Tl_xSb$ photoconductors for various compositions. (b) Responsivity spectra at different temperatures for $In_{0.96}Tl_{0.04}Sb$ photoconductor. Adapted from Ref. [102].

InTlAsSb-Based Devices

Incorporating 'As' as another group-V material and ultimately realizing a quaternary material (InTlAsSb), cut-off wavelength could be further extended to longer wavelengths [97, 103]. World's first observation of photo-response up to 15 *μm* at room temperature could be observed using InTlAsSb based devices. Fig. 22 represents the different photo response spectra at 77 *K* and 300 *K* as shown below.

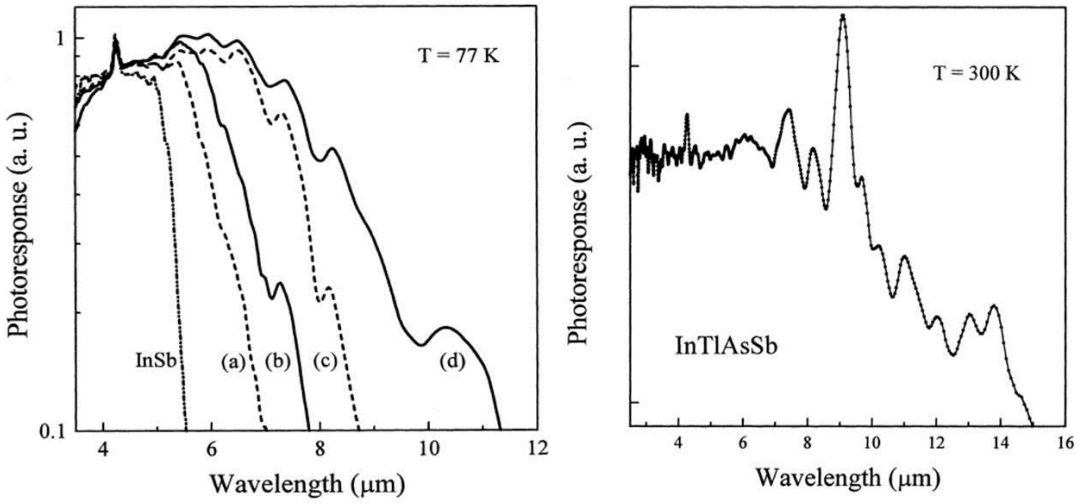

Fig. 22 The normalized infrared spectral photo-response of the InSb, InTlSb and InTlAsSb at 77 *K*. Quaternary sample (b) [(d)] has the identical growth conditions with ternary (a) [(c)] except for the arsenic flux. The 2nd figure corresponds to the room temperature infrared photo-response up to 15 *μm* from the InTlAsSb alloy. Adapted from Ref. [97].

Thus Sb-based alloys could be used to extend the response to the end of the mid infrared range, and even could be extended to much longer wavelength using the proper bandgap engineering.

Type-II Superlattice based THz Optoelectronics

Based on the previous track records of our lab CQD [104, 105, 106, 107, 108, 109, 110] the growth and the realization of the type-II superlattice based infrared detectors are now quite established, which is mostly the world's first demonstration from CQD. In this context, we speculate that the employment of such an InAs/GaSb based type-II superlattice (SL) system might be also considered as a THz emitting as well as detecting structure through proper bandgap engineering. Formation of type-II broken gap structure within InAs and GaSb layers would help in confining the electrons and holes in the consecutive layers separately and an SL system could be established in which the energy difference between the electron states in the InAs layer with the hole states in the GaSb layer falls into the THz window. Consequently, THz optical emission and absorption becomes possible via type II transitions between the spatially separated electron and hole states of different well layers. Therefore, THz optoelectronic devices can be realized from this kind of SL systems. We will, therefore, discuss some of the aspects of the above type-II SL performance in the infrared detection.

InAs/GaSb type-II superlattices consist of materials in the 6.1Å family. The 6.1Å family includes InAs (6.0583Å), GaSb (6.09593Å) and AlSb (6.1355Å) as well, which are closely lattice-matched. Apart from the InAs/GaSb superlattice, another possible structure is the type-II staggered one using InAs/$InAs_{1-x}Sb_x$SL structure; however, due to the lattice mismatching between InAs and $InAs_{1-x}Sb_x$, it obviously requires the strain balancing with small amount of Sb-content. This SL structure is important owing to the absence of Ga, which could lessen the number of defects and consequently the carrier lifetime would increase, leading to higher QE, better dark current and noise.

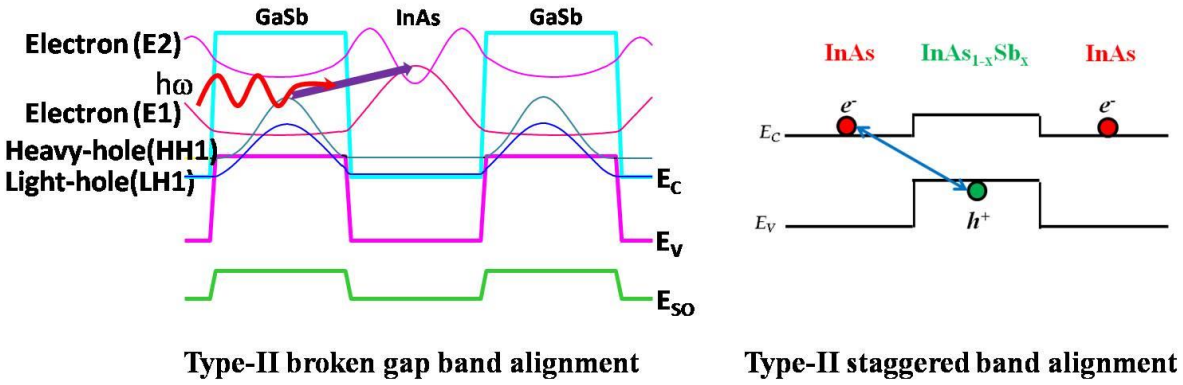

Fig. 23 Type-II broken gap band alignment for InAs/GaSb SL structure and type-II staggered band alignment for Ga-free InAs/$InAs_{1-x}Sb_x$ SL structure.

One of the privileges of the type-II SL is the ability to regulate the detection cut-off wavelength in a wide range. Only through altering the thickness of the ingredient layers, can we precisely control the energy gap of the structure. We have already demonstrated experimentally the photodetection using Type-II InAs/GaSb superlattice structure with cut-off wavelength covering the range of 0.3–32 μm (see Fig. 24). The experimentally measured results could be fitted nicely with the theoretical prediction using Empirical Tight Binding Model (ETBM) [111].

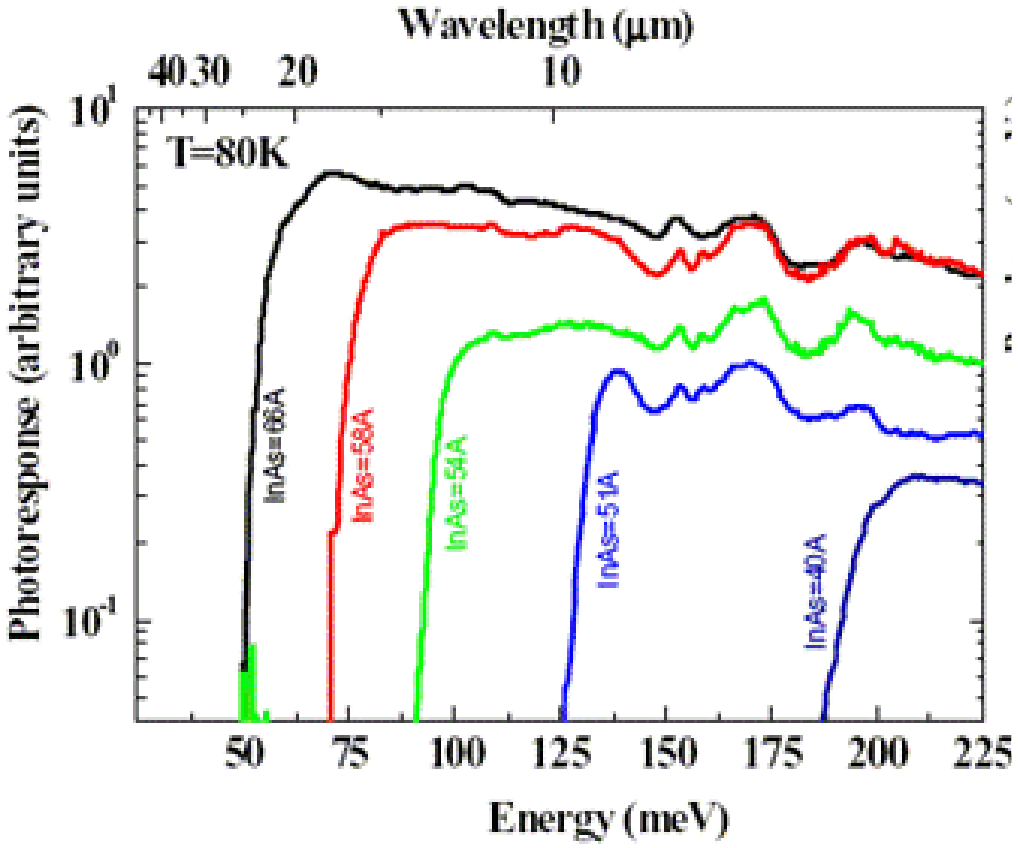

Fig. 24 Spectral response of photodiodes with different InAs/GaSb superlattices. The thickness of the GaSb layer is 40 Å for all the superlattices, while the thickness of the InAs layer varies. Adapted from Ref. [111].

Apart from the simple InAs/GaSb structure, we have developed new device architectures, namely the M-structure superlattice, where electrical noise due to the dark current is sufficiently suppressed using thin AlSb layer within GaSb layer as a blocking layer for both electrons in the conduction band and holes in the valence band. The M-barrier was shown to efficiently suppress both the diffusion current and the tunnelling and of the device, resulting in an order of magnitude reduction of the dark current. Based on the development of material and device architecture, an M-barrier heterojunction was designed for high operating temperature (HOT) mid-infrared detection. The device exhibited a 50% cut-off wavelength of 4.9 μm at 150 K and quantum efficiency above 50% in front side illumination. A MWIR focal planar array (FPA) was developed out of it to demonstrate the real time imaging (see Fig. 25). The image is still recognizable when FPA is

operated at 170 *K*, while uncooled camera can image hot objects such as a soldering iron (not shown here).

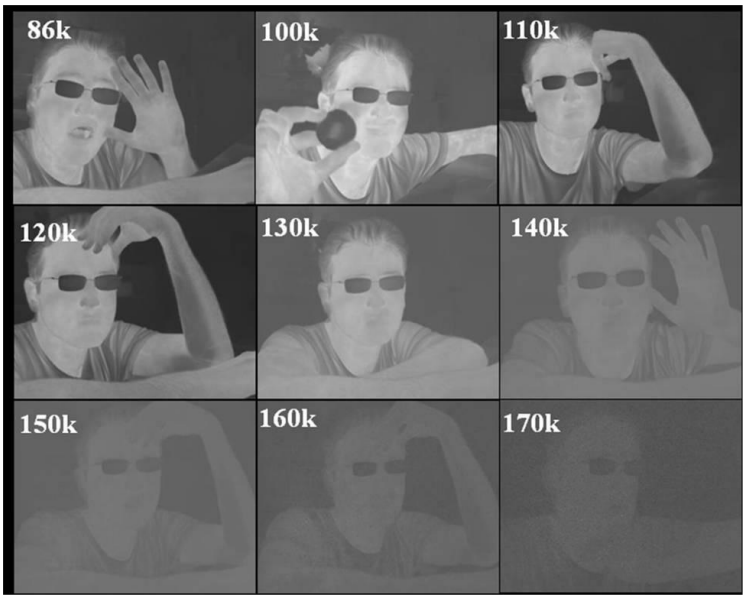

Fig. 25 Human imaging is done at different temperatures using the M-barrier heterojunction based Type-II superlattice MWIR camera. Imaging was carried out at different temperatures from 86 *K* upwards. The image is still recognizable at 170 *K*. Adapted from Ref.[105].

Thus Type-II superlattices are now well established for detection purposes in the MIR range. The good news is that there is still room to engineer the bandgap of such a system to arrive into THz range, which is presently our target and working energy range.

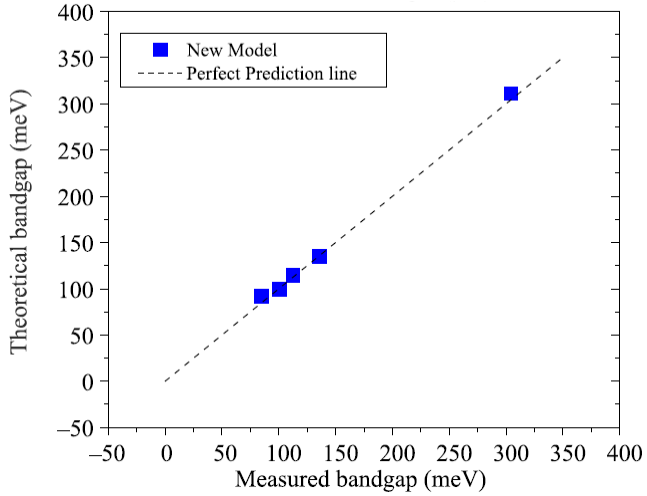

Fig. 26 Comparison of the type−II superlattice band gap predicted by ETBM and experiment. Adapted from Ref. [104].

To start, the band structure of type-II InAs/GaSb superlattices could be calculated using the ETBM method [111]. The method has already proved very efficient for the precise numerical calculations of the bandgap and other energy bands. To get a better agreement with the experimental results, some experimental processes during the growth such as the segregation and subsequent incorporation of materials were also taken into account into the ETBM method. Fig. 26 shows the comparison of the band gap predicted by theory and the experimentally attained values. Clearly the band gap can go to few meV (ultimately falls into the THz window) as can be seen from the predicted line and obviously for that the InAs/GaSb layer widths should be about 6-8/3-8 *nm* range. Therefore, Type-II SL is an appropriate choice to pursue our future research.

InP-Based Devices for THz Optoelectronics

InP-Based Optoelectronics for Telecommunications

This $Ga_xIn_{1-x}As_yP_{1-y}$ material system is just as versatile on InP substrate, and has received a lot of attention thanks to the accessible wavelength range (0.92–1.65 μm) with lattice-matched compositions. These wavelengths (especially near 1.3 and 1.55 μm) are ideal for fiber optic communications, which relies on low-loss and low-dispersion fiber propagation. Lasers and high speed detectors are required for this application.

Some of the initial lasers developed by MOCVD were based on a simple double heterostructure (DH) design. After some time, low threshold current density and long lifetime operation at λ= 1.3 μm and 1.55 μm were demonstrated [112, 113]. These were important demonstrations as they showed that MOCVD could be used to make low power dissipation devices with extremely good reliability.

Even lower power devices were realized by developing buried ridge structure (BRS) lasers. This type of laser geometry utilizes two or more epitaxial growth steps to create a small area GaInAsP active region that is completely surrounded by InP waveguide (Fig. 27a). Both λ= 1.3 and 1.55 μm lasers were demonstrated, with threshold currents of only a few mA and high external quantum efficiencies (30% per facet, Fig. 27b) [57]. Shortly afterward, distributed feedback gratings were added to the device architecture to realize single wavelength emission, which is a critical characteristic for high speed telecommunication sources [114]. Further improvements were then made to laser performance through realization of a separate confinement heterostructure (SCH) GaInAsP/GaInAs/InP, which allows for a more flexible optimization of waveguiding and carrier confinement [115]. For higher power output applications, the BRS structure was also adapted for closely-coupled arrays of emitters, which led to the first GaInAsP/InP phase-locked arrays of λ= 1.3 μm lasers with 600 *mW* output [116].

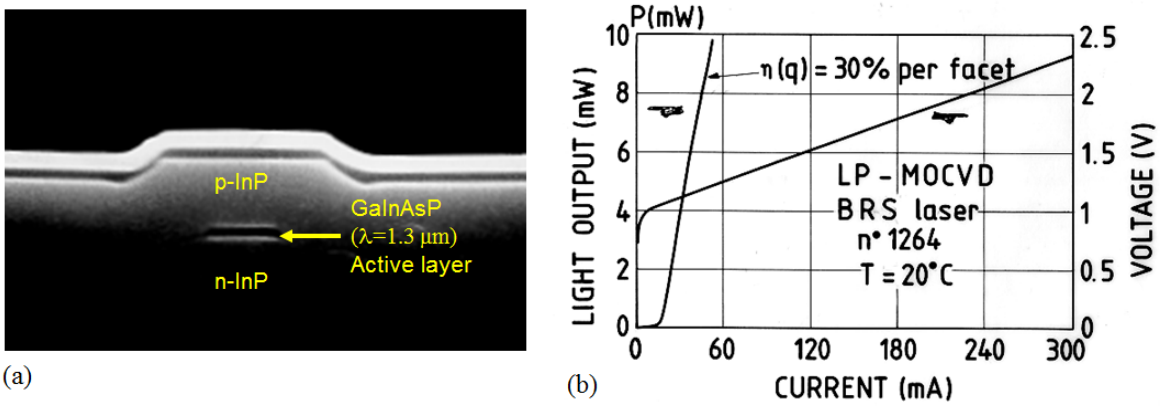

Fig. 27 (a) Cross-sectional image of a BRS laser for emission at λ=1.3 μm. (b) Output power and electrical characteristics for a low power, high efficiency BRS laser. Adapted from Ref. [57].

This flexible material system has also been deposited on other substrates besides InP. The appeal was to make use of larger diameter substrates that could be produced in larger diameters. This would allow for less expensive devices and expanded integration potential. Some of the most important demonstrations were the first GaInAsP-InP lasers grown on GaAs and Si substrates (Fig. 28) [117, 118]. A complementary effort was also successful, which realized the first GaInAs/InP PIN photodiode on Si [119].

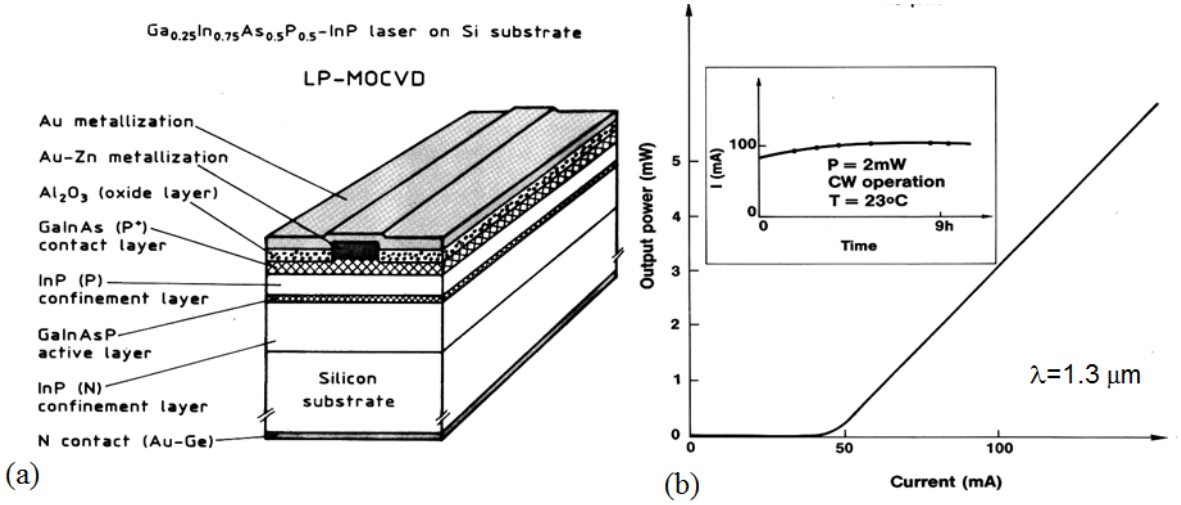

Fig. 28 (a) Schematic diagram of GaInAsP/InP laser grown on a Si substrate. (b) Power as a function of current for a λ=1.3 μm laser on a Si substrate. Inset: Initial life testing of the device in continuous wave (CW) operation. Adapted from Ref. [57].

GaInAsP/InP devices are now the workhorse of the entire telecommunications industry. From tunable lasers to integrated photo-receivers, modern device architectures have grown extremely complex and multi-functional.

InP-Based Intersubband Photodetectors

Similar to the GaAs-based material system, intersubband devices can also be produced with InP-based materials. LWIR n-type QWIPs based on GaInAs/InP have been demonstrated with low dark current and high gain [120]. Various QWIPs were designed using InP barriers with detection wavelengths from 8–20 μm [121]. The binary, Al-free barriers give better electron transport than comparable GaAs/AlGaAs QWIPs. We also demonstrated QWIPs based on GaInAs/AlInAs with detection wavelengths near 4 μm [122].

The first Al-free QWIP based FPA was then demonstrated in 2003 using flip-chip hybridization to a Si-based ROIC [123]. In parallel with this work, due to the complexity of the hybridization process, growth of QWIPs directly on Si substrate was also investigated as a precursor to monolithic integration. High performance GaInAs/InP based QWIPs grown on Si substrate were reported in 2002 [124].

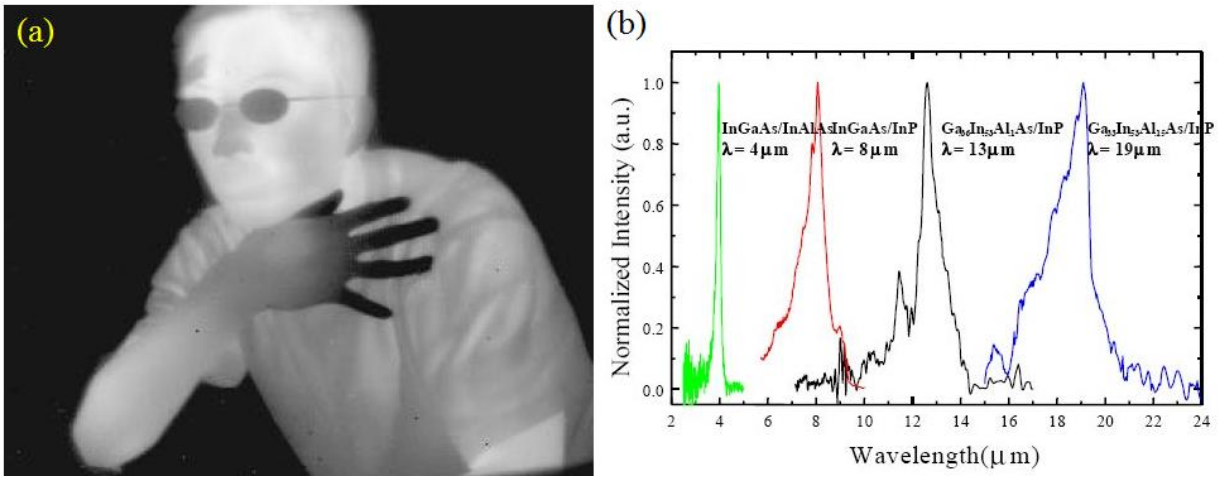

Fig. 29 (a) Image captured from QWIP FPA operating at 100 *K*. (b) Broad spectral coverage demonstrated by various AlGaInAs-based QWIPs.

In parallel with the GaAs-based effort, QDIPs were also developed in the InP material system. A key ingredient in obtaining high performance QDIPs is the formation of the quantum dot (QD) itself. Most commonly, the dots are formed epitaxially via the Stranski-Kranstanov (SK) growth mode in an MBE or MOCVD reactor. Regardless of the growth technique, however, the QDs must be of the appropriate size, have a high density, and be defect-free. Shown in Fig. 30 are characterization results for a single quantum dot and a stack of quantum dot layers produced at CQD. The individual dot shown has a diameter of 50 nm and a height of 5 *nm*.

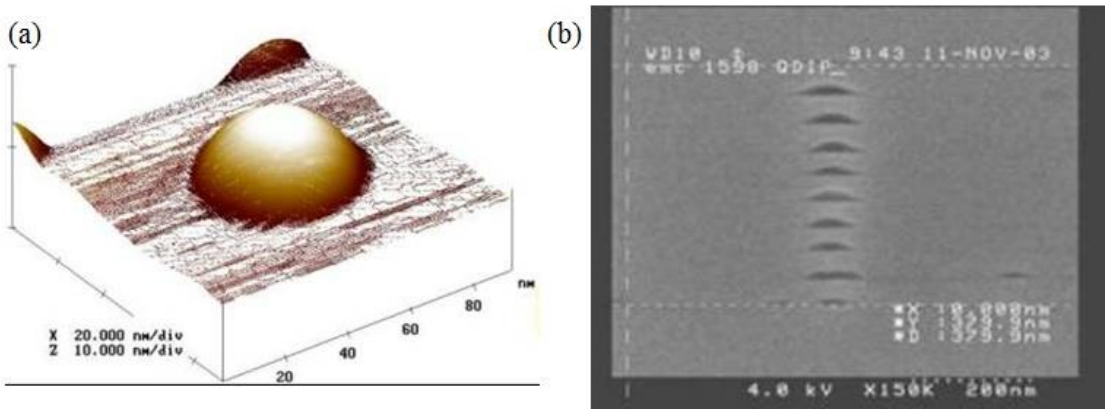

Fig. 30 (a) 3-D projection of quantum dot shape obtained with an atomic force microscope. (b) SEM cross-section of a 10-stack InAs/InGaAs/InP QDIP.

In order to improve performance, specifically operating temperature and quantum efficiency, a variety of materials and device designs were explored. The material system was gradually shifted to InP, similar to the QWIP work done previously, and the structure was refined to a QDWIP design, shown in Fig. 31(a).

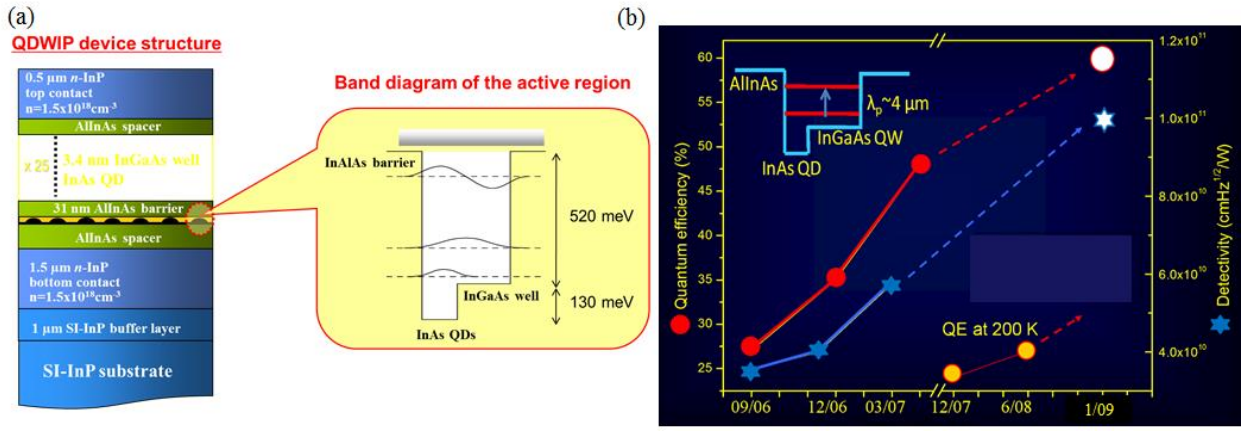

Fig. 31 (a) Example device structure for high efficiency QDWIP. (b) Timeline of improvements to QDWIP quantum efficiency and detectivity demonstrated at CQD.

With this new architecture, rapid improvements were made to device performance, including demonstration of room temperature operation [125]. FPAs were operating up to 200 *K* [126], and single detector quantum efficiency was found to be up to 60% [127]. While this technology is not currently at the level of HgCdTe in some ways, there is still significant potential for high performance operation at high temperature and longer wavelengths. At present, one of the main challenges is to improve the synthesis of the QDs to realize the optimal shape and distribution for detection. Once this is accomplished, the QDWIP is poised to be the dominant next generation detector technology.

InP-Based Quantum Cascade Lasers

The quantum cascade laser (QCL) was also developed primarily in the InP-based material system. It is an intersubband emitter, and has many similarities to the QWIP and QDIP technologies. The primary advantage is that the emission energy is extremely versatile, being controlled by quantum well widths primarily instead of the semiconductor band gap. Light is emitted when electrons make transitions within conduction band quantum wells. This allows the QCL to bypass Auger recombination, which limits traditional interband lasers at longer wavelengths.

After the initial discovery at Bell Laboratories, my group was the first outside Bell Laboratories to demonstrate the QCL, based on the InP material that we had already developed for other devices. Within a month, we demonstrated high power, room temperature QCLs emitting at λ~8.5 μm [128].

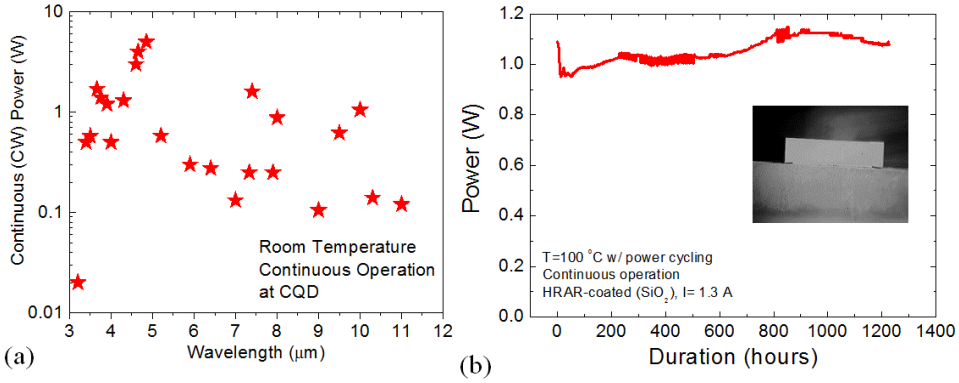

Fig. 32 (a) Summary of CW QCL demonstrations at CQD. (b) High temperature, high power lifetesting results for a CW QCL. Inset shows image of front facet after epilayer-down die bonding.

Over the past 20 years, CQD has demonstrated a wide range of CW QCLs emitting at wavelengths from 3.0 to 11.5 μm [129, 130]. This is illustrated in Fig. 32(a). Some highlights include world records of 21% wall plug efficiency and 5 *W* demonstrated in CW operation for a single laser [131]. Over 53% efficiency has been achieved in pulsed operation at low temperature [132]. We also have extensive experience with power scaling of QCLs, having recently demonstrated discrete lasers with up to 203 *W* of peak power at room temperature [133]. Laser CW reliability has also been tested [134], with over 20,000 *hours* of testing at room temperature, and over 1000 *hours* of high power (1 *W*) testing at 100 ℃. The latter test included power cycling every 30 *minutes* (Fig. 32(b)).

Our group is also one of the pioneers in high power, single mode DFB QCLs. Our world record is 2.4 *W* of near-diffraction-limited single mode output (λ~ 4.75 μm) at room temperature in CW operation [135]. Up to 34 *W* of single mode emission was demonstrated in pulsed mode using a 2-D photonic crystal distributed feedback (PCDFB) architecture [136].

Another technical area of interest is the development of an electrically tunable quantum cascade laser. QCLs have an inherently broad bandwidth that is easily accessible with wavelength-selective

feedback. We have already demonstrated high power single mode lasers (DFB and PCDFB), but they have limited tuning, which requires large arrays of lasers to cover a broad spectral range. External cavity lasers have been developed to fully access the gain bandwidth, but they require a diffraction grating, lenses, and moving components to operate.

Sampled grating distributed feedback (SGDFB) technology provides a single-chip, multi-section alternative that my group has been exploring since 2012. Our first demonstration showed up to 50 cm^{-1} of electrical tuning with a single laser in CW operation [137]. Advanced grating design has led to pulsed tuning of individual lasers with 243 cm^{-1} of tuning [138], though more recent, unpublished work has increased this record to >350 cm^{-1}. This work was also instrumental in demonstration of tunable THz emitters (see Fig. 41).

More recent effort has focused on further integrating tunable lasers for additional power and tuning range. A SGDFB laser with an integrated amplifier has demonstrated a tuning range of >120 cm^{-1} with >1 W (>5 W) output power in CW (pulsed) operation [139]. In addition, arrays of SGDFB lasers, integrated with a broadband laser design [140] and an integrated beam combiner, have shown tuning over 550 cm^{-1} in the 6.2–9.4 μm wavelength range [141]. An illustration of our tunable laser demonstrations is given in Fig. 33. Another recent innovation was the demonstration of electrically-controlled beam steering. A SGDFB laser integrated with beam forming components, grating outcoupler, and heater has been demonstrated with up to 17.9 degrees of beam steering [142]. The 3 dB bandwidth for steering is >7 kHz.

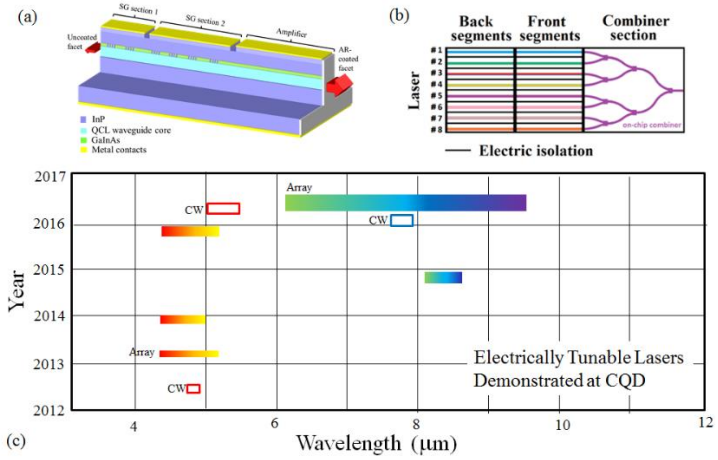

Fig. 33 (a) Device structure of SGDFB with integrated amplifier. (b) Top view of SGDFB array layout with integrated beam combiner. (c) Summary of electrically tunable laser demonstrations at CQD.

Though the QCL is now available commercially, the price is not easily accessible for most people. Individual lasers sell for several thousand dollars at this point, and it is of significant interest to reduce costs by modifying the manufacturing technique. The growth technology itself is not a significant issue as we have demonstrated comparable performance with both GSMBE and MOCVD techniques. Moving towards larger wafers and multi-wafer production systems is

certainly a step in the right direction as well. Another aspect, however, is reduction of labor costs. Most QCLs require cleaving, mirror coating, and full packaging before they can be evaluated. This problem was solved in the near-infrared by moving toward vertical cavity surface emitting lasers (VCSELs), which can be fabricated and evaluated on a wafer scale due to the absence of a cleaved mirror facet. An automated probe station can be used to rapidly detect bad devices prior to die singulation and packaging.

Unlike interband lasers, the QCL emitted light is polarized in a way that does not allow a practical vertical cavity laser. However, we are developing other technologies, such as the ring laser, which uses a second order grating to couple light vertically out of the laser (Fig. 34(a)). The ring laser does not require a cleaved facet, and is compatible with wafer-scale testing. We have previously demonstrated high power (>0.5 *W*) CW operation from ring lasers (Fig. 34(b)) [143]. Recent improvements have also allowed us to demonstrate low divergence with improved beam quality (Fig. 34(c)) [144]. This simplifies light collection and fiber coupling, which will reduce packaging costs. We are also investigating coupled ring arrays for coherent power scaling. A peak pulsed output power of 3.1 *W* has been obtained from a coupled ring QCL pair (Fig. 34(d)). A surface emission modality, with all of the same benefits, was also utilized for the recent beam steering demonstration [142].

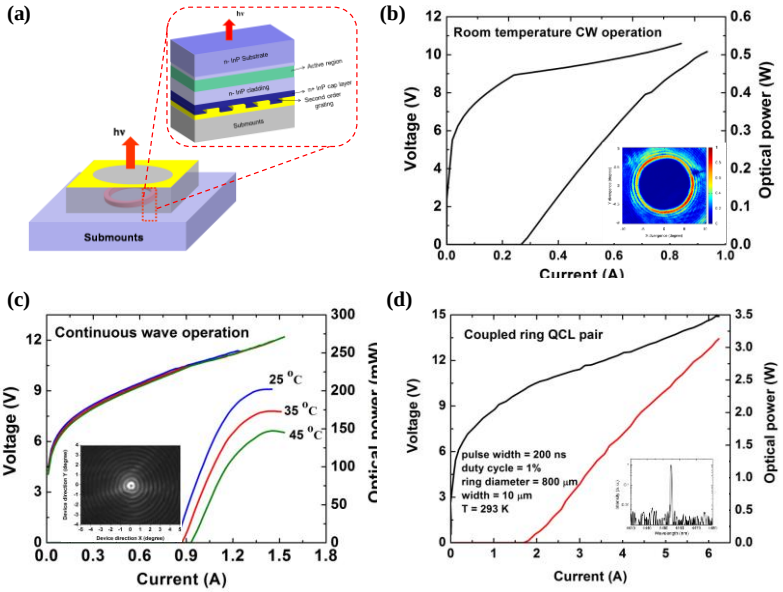

Fig. 34 (a) Schematic three-dimensional surface emitting ring QCL device representation. (b) P-I-V curve of single ring QCL with buried grating design in room temperature CW operation. Inset shows the measured far-field. (c) P-I-V curve of single ring QCL with surface grating design in room temperature CW operation. Inset shows the measured far-field. (d) P-I-V curve of coupled ring QCL pair in room temperature pulsed mode operation. Inset shows the single mode spectrum.

Overall, the quantum cascade laser (QCL) is an important laser source in the mid-infrared range. The past twenty years have witnessed its tremendous development in power, wall plug efficiency,

frequency coverage and tunability, beam quality, as well as various applications based on QCL technology.

Room Temperature THz Emitters Based on QCL Technology

In the THz range, GaAs-based QCLs have emerged as the most powerful semiconductor THz sources. However, the working temperature is still below 200 *K*. On the other hand, THz sources based on intracavity difference frequency generation (DFG) in mid-IR QCLs are developing rapidly in the recent years, and become the only semiconductor light source that emits over 1-6 *THz* range with optical power up to mW at room temperature [80]. A QCL active region designed for having strong coupling between the lower lasing levels and injector levels would possess a large nonlinear susceptibility $\chi^{(2)}$, resulting a strong THz emission by means of DFG between two strong longitudinal modes within the cavity [145]. Thus, this type of THz source is free from the temperature limitation suffered by the THz QCLs based on direct optical transition, and ideally its working temperature is only limited by the mid-IR QCL which can work well even above 100°C [146], and can be tuned over a broad waveguide range with broadband heterogeneous active region design [147]. It not only shares the common features of the mid-IR QCLs which are mass reproducible, room temperature operation, low cost, compact size, and high efficiency, but also carries the potential of delivering THz emission with high power in a wide frequency range.

Below, we present our recent breakthroughs in high power and continuous wave (CW) THz DFG QCLs, discussed in details in the following sections, on nonlinear active region, composite DFB waveguide design, epi-down Čerenkov phase matching scheme, high THz power operation, room temperature continuous wave THz operation, widely tunable THz DFG QCL sources, and surface emitting THz DFG QCL sources and future trend.

Design of nonlinear active region. For a mid-infrared (mid-IR) QCL featuring a giant second-order nonlinear susceptibility ($\chi^{(2)}$) for DFG in its active region and dual wavelength operation, THz emission can be generated from an extremely compact device at room temperature. The THz power strongly relies on high powers from the mid-IR sources (W_1, W_2), and a giant $|\chi^{(2)}|$. Dual-core active regions featuring double-phonon-resonance (DPR) and bound-to-continuum (BTC) depopulation schemes have been used for the first generation of THz sources based on DFG QCLs [148, 149]. Among the two core designs, only the BTC core is designed with a giant nonlinear susceptibility and the DPR core merely acts as a mid-IR source with little THz generation. Meanwhile, the mid-IR QCL technology has made a tremendous progress in power and efficiency, thanks to the improved material quality, waveguide, and especially the elaborate quantum designs [150, 151, 152, 153]. Out of these, QCLs based on the single-phonon-resonance (SPR) design have demonstrated the highest power and efficiency in the shorter mid-IR wavelength range (4-6 μm) [131]. The strong coupling of the lower lasing state and the upper injector state indicates that the SPR design in the long mid-IR wavelength range can be designed with giant nonlinearity without much compromise on its high power feature [154].

Fig. 35(a) shows a lattice matched $Ga_{0.47}In_{0.53}As/Al_{0.48}In_{0.52}As$ SPR structure at a wavelength of λ_1~9.0 μm designed for THz DFG. The band structure is shown at the high fields when the maximum mid-IR powers are expected. The state 1 is separated by about one optical-phonon energy from state 2, which helps to depopulate state 2 with ultrafast optical-phonon scattering. The lifetime of the upper lasing state 3 caused by phonon scattering is increased from 0.39 *ps* for the BTC design to 0.46 *ps* for the SPR design, while the lifetime of the lower lasing state 2 is maintained at 0.1 *ps*. The major contributions to the THz DFG nonlinearity stem from the adjacent states 2 that are within 10–20 *meV* of the lower lasing state 2. The electron density in the states involved in DFG can be estimated with a simplified rate equation model by applying the lasing threshold condition ($G_{gain}=(\alpha_m+\alpha_w)/\Gamma$) at which the champing occurs. G_{gain}, α_m, α_w, and Γ are gain, mirror loss, waveguide loss, and confinement factor, respectively. Given the waveguide loss of 8 cm^{-1}, mirror loss 2.3 cm^{-1} for a 3 *mm* long HR-coated cavity, and confinement factor of 0.4, the electron densities in the upper lasing level, the lower lasing level 2 and its adjacent levels contributing to DFG are calculated to 2.0×10^{15}, and 2.1×10^{14}, 1.1×10^{14}, 4×10^{14} cm^{-3}, respectively. The nonlinear susceptibility is estimated to be $|\chi^{(2)}|=3.97\times10^4$ *pm/V* at 4 *THz*.

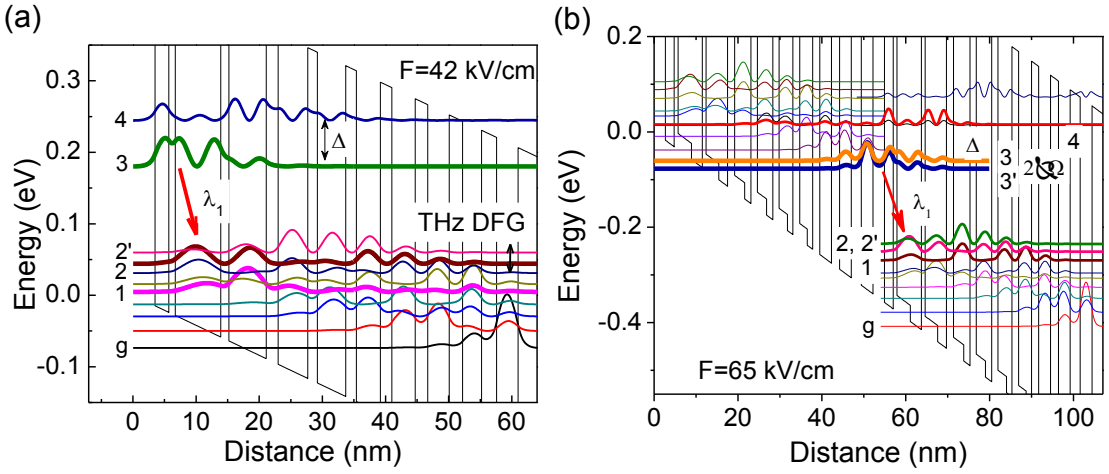

Fig. 35 (a) Band structure of a SPR structure at λ~9 μm with large nonlinear DFG susceptibility based on lattice matched $Ga_{0.47}In_{0.53}As/Al_{0.48}In_{0.52}As$ material system. (b) Band structure of a strongly coupled SPR structure at λ~7.8 μm based on strain-balanced $Al_{0.63}In_{0.37}As/Ga_{0.35}In_{0.65}As/Ga_{0.47}In_{0.53}As$ material system

The limited conduction band offset (~0.5 *eV*) for the lattice-matched design results in an energy spacing of ~240 *meV* between the upper laser level and the continuum states located above the barriers, which is not able to confine the electrons in the upper laser level effectively, and induces significant thermally activated carrier leakage into the continuum. This leads to less efficient performance of the devices compared to the state-of-art shorter-wavelength counterparts. To further improve the THz performance, a nonlinear SPR active region based on the strain-balanced $Al_{0.63}In_{0.37}As/Ga_{0.35}In_{0.65}As/Ga_{0.47}In_{0.53}As$ material system is designed [155]. The band structure is shown in Fig. 35(b). The targeted wavelength is λ~7.8 μm. The inserted $Ga_{0.47}In_{0.53}As$ layers are used to balance the material strain within one stage. The conduction band offset is enhanced to

~0.74 *eV*. In the present strain-balanced design with a diagonal optical transition scheme, the increased conduction-band offset and interface roughness increases the broadening the oscillation linewidth to ~15–20 *meV*, compared to that of ~10 meV for the lattice-matched active region design [154]. This allows for a stronger coupling design between the injector and upper lasing level. A high coupling strength with an energy splitting of $2\hbar\Omega$ = 16.5 *meV* is calculated for the present structure. This strong-coupling design not only effectively improves the carrier tunnelling rate into the upper lasing state 3, but also enhances the DFG nonlinear susceptibility $\chi^{(2)}$ [156]. Normally, the optical nonlinearity is engineered by the adjusting the injector barrier thickness so that the lower laser state 2 couples with its neighbouring levels 2' with an energy spacing of 14–17 *meV* (3.4–4.1 *THz*). Here, the strong-coupling design with an energy splitting of 16.5 *meV*, provides another scheme to the total nonlinear susceptibility. Given a threshold gain g_{th} = 5 cm^{-1} for CW operation, a total nonlinear susceptibility of $|\chi^{(2)}|= 2.0\times10^4$ is obtained from the present design. This is comparable to the value of 2.6×10^4 *pm/V* from the previous lattice-matched active region design at λ~9 μm with a higher threshold gain [157].

Composite DFB waveguide and epi-down Čerenkov phase matching scheme. In a typical multimode Fabry-Pérot (FP) cavity, the light intensity spreads out among different mid-IR frequencies, and the total power is the sum over many small W_i components. As such, the product W_iW_j will be small and the THz spectrum will rather broad ($\Delta\nu$ ~ 0.5–1 *THz*). In order to purify and tune the THz spectrum, all the mid-IR power needs to be concentrated on the two mid-IR frequencies with single mode operation, and their frequency positions need to be controllable and tunable. The most straightforward way to this end is to use the composite DFB grating with wavelength components to purify and tune the mid-IR spectra [149]. While the design strategy of dual-period DFB grating shares some similarity to the single-period DFB like sufficient coupling strength for single mode operation, balancing the coupling strength, waveguide loss, and modal gain of the two grating components is of special importance. Fig. 36(a) shows the scanning electron microscope (SEM) pictures for two composite DFB gratings designed for 1 *THz* and 4 *THz*, respectively. Double-exposure holographic lithography or electron-beam lithography has been used [149, 157]. The exposing dose ratio between the two exposures is adjusted to balance the coupling coefficients (κ_1 for λ_1 and κ_2 for λ_2) and reflection intensity between the two wavelength components. As shown in Fig. 36(b), roughly similar intensity is obtained by using the same exposure doses for the double e-beam exposure, which naturally balances the coupling strengths for the two wavelengths via their different grating duty cycles due to the different period components. Around a surface grating depth of 200 *nm*, similar coupling coefficients of ~10 cm^{-1} are obtained for the two wavelengths. This grating design offers sufficient coupling strength for 2–3 *mm* cavities with high-reflection (HR) coatings.

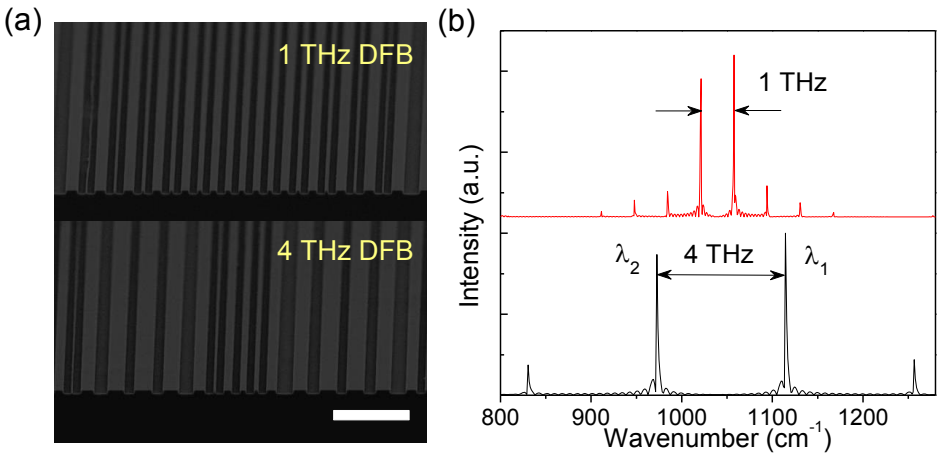

Fig. 36 (a) SEM images and (b) the Fourier analysis of the composite DFB gratings with 1 and 4 *THz* frequency spacing. The white bar in (a) corresponds to 4 μm.

To achieve a high mid-IR-to-THz power conversion efficiency, the phase mismatching should be close to zero to obtain an effective nonlinear interaction. In a waveguide with modal phase matching scheme, due to a faster frequency dependent effective index in the THz range with respect to the mid-IR index ($n_{mid\text{-}IR}$), the modal phase matching is only satisfied within a relatively narrow frequency range for a certain waveguide [158]. In contrast to this narrow-band phase matching scheme, the Čerenkov scheme has been used as an effective broad-band phase matching method for THz generation in the externally pumped optical rectification or DFG setups [159, 160]. Čerenkov nonlinear emission occurs when the nonlinear polarization wave propagates at a higher phase velocity compared to that of the nonlinear radiation, as shown in Fig. 37(a). For THz DFG in QCLs, the waveguide for Čerenkov phase matching scheme can be designed so that the THz refractive index (n_{THz}) in the QCL substrate is higher than the mid-IR group effective refractive index ($n_{mid\text{-}IR}$). In this case, the fundamental mid-IR wave propagates faster than the second-order DFG THz wave, and the THz wave travels at an angle $\theta_C=\cos^{-1}(n_{mid\text{-}IR}/n_{THz})$ with respect to the mid-IR wave, θ_C is the Čerenkov angle. This can be achieved by replacing the n-doped InP substrate with a semi-insulating InP substrate where n_{THz} (~3.47–3.71) larger than $n_{mid\text{-}IR}$ (~3.35) is fulfilled automatically in the 1-6 *THz* range. This broad-band Čerenkov phase matching scheme is used to take full advantage of the wide bandwidth of the THz nonlinear medium based on SPR design. The QCL epilayer structure together with a 200-*nm* InGaAs bottom contact layer is grown by gas-source molecular beam epitaxy on a semi-insulating InP substrate. The sample was processed into ridge waveguide by dry or wet etching with a ridge width of 20–25 μm. The front facet is polished into 30° to facilitate the Čerenkov THz output.

Since the THz light is coupled out from the substrate with a facet-polished angle of 20–30° for Čerenkov phase matching scheme, the ideal scenario is to use a thick substrate to couple out as much light as possible. In the experiments, the 350 μm thick substrate is normally not polished, however, thick substrate will lead to inefficient heat removal in the epilayer-up mounting scheme, and a less efficient current injection scheme due to the single-side current injection through a thin

layer of bottom contact. This results in the limited THz power output in spite of the relatively high power conversion efficiency [154, 161]. Fig. 37(b) (upper) show the temperature distributions of an epilayer-up mounted QCL with an asymmetric contact pattern near the front facet. The polished angle of the facet is set to be 30˚. Clearly, the epilayer-up mounted Čerenkov device suffers severely from thermal and electrical issues, as the heat near the front facet is not effectively dissipated. Moreover, the non-uniform electrical distribution across the active region induces non-uniform current injection with the electrical field varying over 2-4 *kV/cm*. To address these two issues, double-sided current injection and epilayer-down mounting on a patterned submount are proposed, as shown in Fig. 37(c) [162, 163]. The heat dissipation is improved significantly as shown in Fig. 37(b), and the electrical distribution is much more uniform with electrical field variation less than 0.5 *kV/cm* in the lateral plane of the active region. In the experiment, AlN or diamond submounts are prepared following the patterns compatible with the contacts of the device for epi-down bonding. Fig. 37(d) is a SEM image of an epi-down mounted Čerenkov THz device.

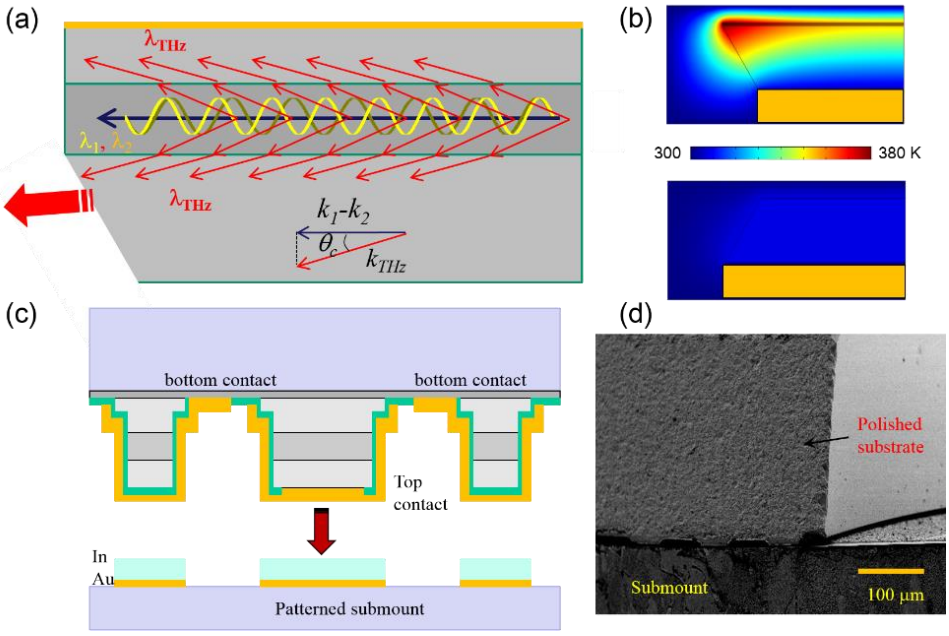

Fig. 37 (a) Schematic of Čerenkov phase matching in a mid-IR quantum cascade lasers. (b) The thermal distributions of the epi-up and epi-down mounted Čerenkov devices. (c–d) Schematic of the epi-down mounting scheme and the SEM image of an epi-down mounted device. Adapted from Ref. [163].

High power DFG QCL THz sources. Ever since from the first demonstration, THz sources based on DFG QCLs have strived for high power operation at room temperature. Through the above systematic optimizations to the nonlinear active region, DFB waveguide, phase matching scheme, and device bonding technique, the THz output power experiences an exponential increase in the recently years, as depicted in Fig. 38(a). Currently, the highest THz power up to 1.9 *mW* with a conversion efficiency of 0.8 mW/W^2 is achieved from a HR coated, 3 *mm* long, 23 μm wide composite DFB laser epilayer-down mounted a patterned diamond submount, as shown in Fig.

38(b). The measured THz power is not corrected with any collection efficiency. The maximum THz power wall plug efficiency for this device reaches to 0.7×10^{-5}.

Spectral emission is single mode at 3.5 *THz* wish SMSR as high as 30 *dB* as shown in Fig. 38(c). The far field testing indicates that the device exhibits a good beam profile with divergence angles of 12.5° in the vertical direction and 36° in the lateral direction with a dual-peak distribution. Ideally, the far field pattern of the Čerenkov THz emission inside of the QCL waveguide should be a conical shape with the cone angle equal to the Čerenkov angle because of the much longer emitting wavelength respecting to the width of the QCL waveguide [157]. This indicates that only part of this radiation cone is able to be coupled out through the polished substrate facet limited by the Brewster's angle $\theta_B \approx \pm 16.5°$, which is inferred from $\theta_B = \sin^{-1}(n_{air}/n_{InP})$ with n_{air} =1, and n_{InP} =3.5. Considering another 30% reflection to both the mid-IR and THz emissions, the outcoupling efficiency of the emitted THz power with respect to the generated power is as low as 15%. Given the maximum recorded 1.9 *mW* output power, the total generated THz power in that device is estimated to be ~12 *mW*. Therefore, there is a great potential for THz power enhancement when an efficient THz outcoupler is applied to the THz waveguide. By enlarging the outcoupling aperture with a Si prism to allow for more THz light to be coupled out from the substrate or extract the THz light from the entire cavity via diffraction grating, even higher THz power and efficiency in a wider spectral range in pulsed and CW modes can be obtained [164]. This is of special importance to high THz frequency generation (>4.5 *THz*) where the phonon absorption in the semi-insulating InP substrate plays a leading role to the THz absorption prior to outcoupling. On the other hand, the power a mid-IR QCL has been scaled up to 200 *W* [133]; with a similar strategy, the THz power can be further enhanced to tens of mW by scaling the device area.

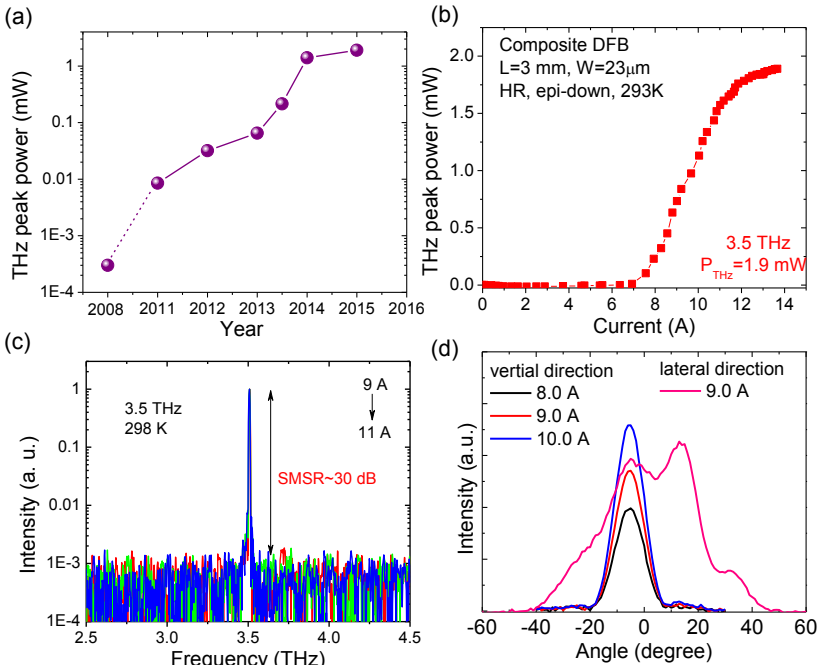

Fig. 38 (a) Recent demonstrated THz power records of the THz sources based on DFG QCLs at room temperature as a function of year. THz power (b), spectra (c), and far field (d) as functions of currents for a high power THz sources based on DFG QCLs. Adapted from Ref. [163].

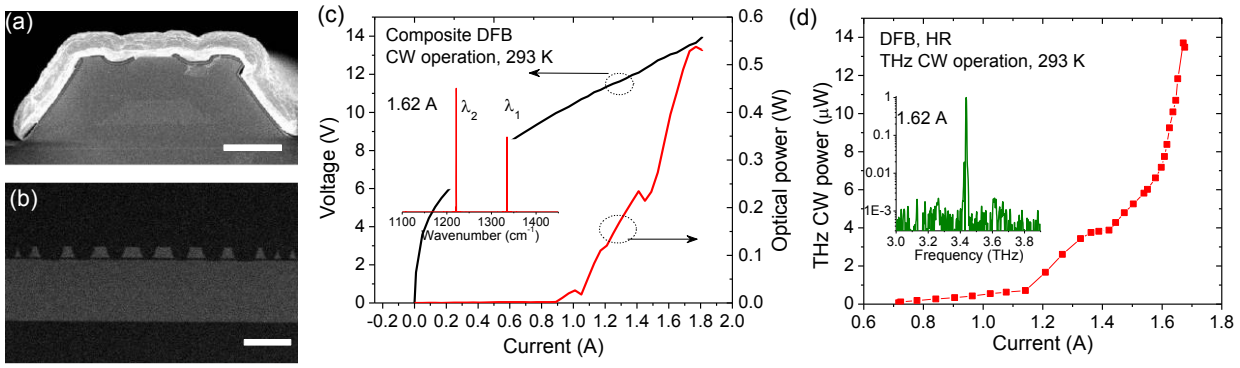

Fig. 39 SEM images of a buried ridge (a) and buried composite DFB grating waveguide (b). The white bars in (a) and (b) corresponds to 10 and 2 μm, respectively. (c) Power-current-voltage (*P-I-V*) of a composite DFB THz device at room temperature CW operation. Inset: CW lasing mid-IR spectrum at 1.62 *A*. (d) THz CW power as a function of current. Inset: CW THz spectrum at 1.62 *A*.

Room temperature continuous wave THz DFG QCL sources. While a lot of effort has been devoted to improve the THz power and frequency tuning range of the THz sources based on DFG in QCLs, the capability of CW operation at room temperature is of utter importance to wide application and commercialization [157, 165]. Nevertheless, room temperature CW operation has been difficult to be achieved for the following reasons. First, the design priority has been to achieve for a large nonlinear susceptibility for THz generation. However, this may compromise the mid-IR performance. Second, in order to obtain a large population inversion, the doping of the structure is much higher than a typical mid-IR QCL, which results in a high threshold current density, precluding room temperature CW operation. Third, in order to obtain high peak power, the waveguide structure is often wider than a typical mid-IR QCL, which poses a big challenge for thermal management. These issues are recently addressed by utilizing a low-loss buried-ridge waveguide design and highly dissipative epi-down mounting scheme (Fig. 39(a)), room temperature continuous wave (RT-CW) operation at 3.6 *THz* was demonstrated with a continuous power of 3 μW [157].

To further enhance the THz CW power, a new strong-coupled strain-balanced quantum cascade laser design for efficient THz generation based intracavity DFG with an epi-down mounting scheme. A single-phonon resonance active region made from a composite strain-balanced $Al_{0.63}In_{0.37}As/Ga_{0.35}In_{0.65}As/Ga_{0.47}In_{0.53}As$ active region is designed with strong coupling of $2\hbar\Omega$ =16.5 *meV*. The concurrent advantage of this strong coupling design is that the upper laser level spreads more into the injector region because of the thin injection barrier, so that the radiative transition is more diagonal, which increases not only increase the slope efficiency with elevated upper laser level lifetime, but also increase the gain spectral width, as evidenced by the electroluminescence (EL) measurement results [155]. The FWHM of 380 cm^{-1} is even broader than the previous dual-core lattice-matched active region with a FWHM of ~330 cm^{-1} in the 9-11 μm wavelength range, which makes this homogenous active region able to provide a sufficiently wide gain to support the 1-5 *THz* emission [154].

In CW operations, a 4 *mm* long composite DFB device emits up to 0.53 *W* with threshold current densities of 1.87 kA/cm^2, as shown in Fig. 39(b).The inset is the CW lasing spectrum at 1.62 *A*. Stable dual-wavelength operation at λ_1=7.46 μm and λ_2=8.15 μm with a frequency spacing of 3.4 *THz* is observed. For a FP device with identical geometry, a maximum power of 3 *W* and threshold current density of 1.95 kA/cm^2 in pulsed mode operation, and a maximum power of 1.1 *W* and a threshold current density of 2.2 kA/cm^2 in CW operation are demonstrated, respectively. The maximum wall plug efficiencies (WPEs) are 10% and 4% for pulsed mode and CW operations, respectively. Fig. 39(c) is the THz power of the composite DFB QCL in CW operations at 293 *K*. Maximum CW power of 14 μW with conversion efficiencies of η=0.35 mW/W^2, and THz WPE of 0.8×10^{-6} is obtained. The superlinear increase in CW THz power in Fig. 39(d) is due to the rapid power increase in λ_1 and dramatic power balancing between λ_1 and λ_2 in the current range of 1.45-1.68 *A*. The maximum CW powers are much higher than previous demonstrations in Ref. 157 despite that the conversion efficiency is lower due to the relatively lower nonlinearity induced by the reduced threshold gain. As a result, the THz CW WPE is about one order of magnitude higher than the previous demonstration. The increased THz power and WPE are mainly attributed to the enhanced mid-IR power and efficiency of the strong-coupled strain-balanced active region design.

This initial attempt based on strain-balanced active region design indicates a great promise for CW THz power enhancement. Considering the state-of-art QCL performance of 21% and 5.1 *W* in CW operation and the potential for outcoupling efficiency enhancement, THz CW power up to sub-mW level is achievable [131].

Widely tunable THz DFG QCL sources. A compact, high power, room temperature terahertz source emitting in a wide frequency range will greatly benefit terahertz system development for applications in spectroscopy, communication, sensing, and imaging. The THz source based on DFG in QCL has been designed with a broad gain spectrum and a giant nonlinear susceptibility over a broad THz frequency range [154]. Recently a tuning from 1.2 to 5.9 *THz* based on DFG in QCLs has been demonstrated using an external cavity [164]. To achieve monolithic tuning which has a wider application, composite DFB arrays were demonstrated. The device consists of an array of composite DFB devices with different grating period designs emitting at different THz frequencies, as shown in Fig. 40(a).

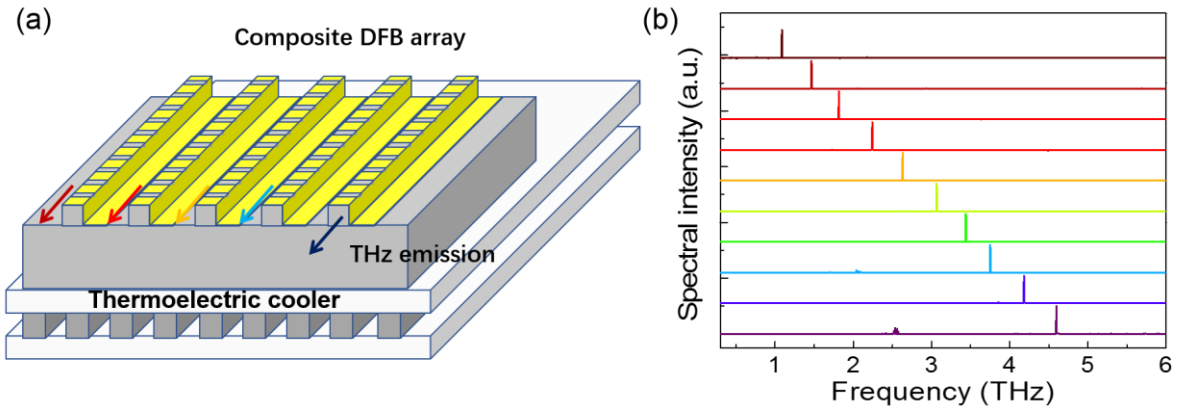

Fig. 40 (a) Schematic of composite DFB array, (b) THz emitting spectra from 1.0 to 4.6 *THz*.

Single mode operations from 1.0 to 4.6 *THz* are demonstrated from a composite DFB array as shown in Fig. 40(b), with a frequency step-tuning range (Δv) of 3.6 *THz* and a mean SMSR above 30 *dB*. This range represents 1.28 *times* that of the central frequency. For each of the device, the THz spectral position is pretty stable with respect to the temperature or current changes. The average current tuning rate is about 1 *GHz/A* and the linewidth is about 6-8.6 *GHz*, which is mainly limited by the resolution of the FTIR spectrometer (0.125 cm^{-1}). Much wider, continuous tuning can be achieved by employing the dual-section sampled grating design for each emitting elements [137, 138].

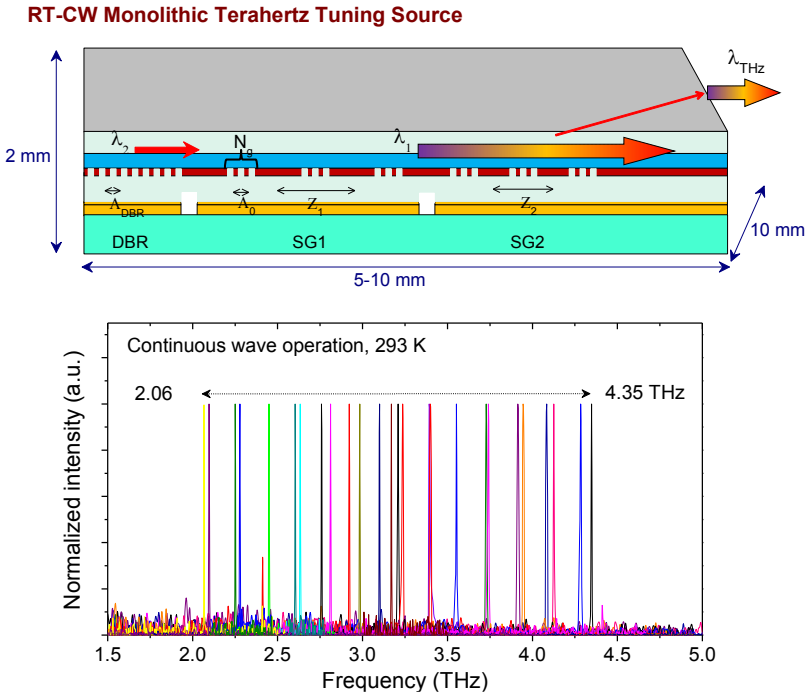

Fig. 41 (a) Schematic of SGDFB-DBR waveguide design for THz tuning. (b) Combined tuning of 2.06-4.35 *THz* of the two epi-down mounted THz SGDFB-DBR devices. Adapted from Ref. [155].

To achieve wide THz tuning from a single THz emitter, we have recently demonstrated a monolithic tunable THz source based on multi-section sampled-grating distributed feedback-distributed Bragg reflector (SGDFB-DBR) design, as shown in Fig. 41(a) [166]. Both the two sampled-grating (SG) sections are sampled with a very short grating section (Λ_0= 1.22 μm, N_g= 15) for 7 *times*. Here N_g is the grating number in one short section. The sampling periods Z_1=207 μm and Z_2=185 μm were used for the front and back SG sections, respectively. To enhance the power performance, the front SG section was further elongated with a 1.5 *mm* unpatterned section for power amplification. Laser bars with 6.3 *mm* cavity length were cleaved, containing one 1 *mm* DBR section (Λ_{DBR}=1.329 μm) on the back, one 2 *mm* SG section (SG1) in the middle, and one 3.3 *mm* SG section plus the amplifier (SG2) in the front.

These three-section devices are then epi-down mounted on patterned diamond submounts for CW measurements. The measured THz tuning spectra are presented in Fig. 41(b). A wide frequency tuning from 2.06 to 3.17 *THz* with a step of 185 *GHz* by changing the DC current on SG1, and 2.09 to 3.10 *THz* with a step of 168 *GHz* by changing the DC current on SG2, are achieved respectively. Another device with a slightly different grating period designs of Λ_0=1.196 μm and Λ_{DBR}=1.36 μm targeting a larger frequency spacing, exhibits a full tuning range of 3.2 to 4.35 *THz*, as shown in Fig. 41(b). The combined tuning range for the two devices is 2.29 *THz*. The SMSR ranges from 12 to 25 *dB* in the tuning range measured with an uncooled far-infrared DTGS detector. In the tuned THz frequencies, the THz output power ranges from 0.6 μW at 2.06 *THz* to 4.2 μW at 3.42 *THz*. The conversion efficiency peaks around 3.0–3.5 *THz* with η_{max}=0.36 mW/W^2 at 3.2 *THz*.

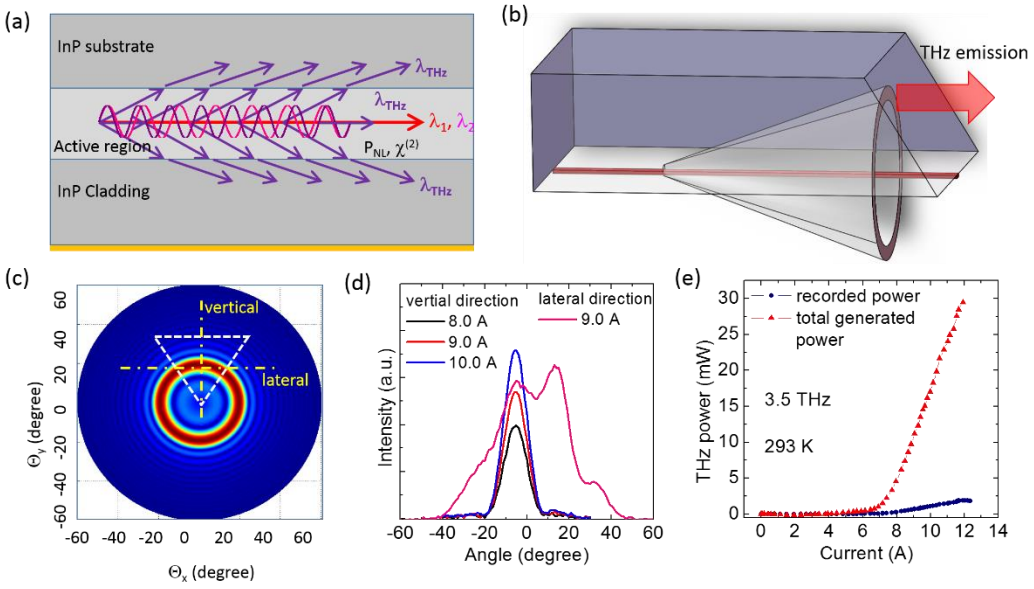

Fig. 42 (a) Schematic epi-down mounted Čerenkov phase matching in a slab waveguide. (b) Čerenkov radiation cone in a ridge waveguide with a polished facet for edge emission. (c) Calculated Čerenkov radiation cone inside of the cavity. (d) Tested THz far field distributions in vertical and lateral directions. (e) Tested THz power up 1.9 *mW* and estimated total THz power generated inside of the cavity.

Surface emitting THz sources and future trend. All the above devices are based on edge emission scheme by polishing InP substrate into 20–30° for THz out-coupling. However, this type of edge emission scheme has a limited out-coupling scheme. Fig. 42(a) shows the schematic of the Čerenkov THz generation based on DFG in a QCL slab waveguide. When the slab waveguide has a width much wider than the THz wavelength λ_{THz}, the THz wave will be emitted in the form of a plane wave into the upper and low InP waveguide layers with a Čerenkov angle $\theta_C=\cos^{-1}(n_{mid\text{-}IR}/n_{THz})\approx 22°$. Here $n_{mid\text{-}IR}$ and n_{THz} are mid-IR and THz group index of the waveguide.

In previous demonstrations, the QCL waveguides have finite ridge widths of 10-20 μm, which is much which is smaller than THz wavelength of 50-300 μm (corresponds to 1-6 *THz* frequencies). As a result, the THz radiation is emitted from ridge-waveguide QCLs in a cone of angle into the substrate, instead of a plane wave in a slab-waveguide model, as shown schematically in Fig. 42(b). Numerical calculation of this Čerenkov emission cone is presented in Fig. 42(c). The evidence of Cherenkov emission cone in THz DFG–QCLs is shown in Fig. 42 (d), and was first reported in Ref. 157. In the edge-emission scheme with a polished facet shown in Fig. 37(a), however, only a portion of the Čerenkov emission cone can be out-coupled, as indicated by the triangular in Fig. 42(c). The THz light can only be collected within the Brewster angle $\theta_B\approx\pm 16.5°$, which is inferred from $\theta_B=\sin^{-1}(n_{air}/n_{InP})$ with $n_{air}=1$, and $n_{InP}=3.5$. Considering another 30% reflection to both the mid-IR and THz emissions, the outcoupling efficiency of the emitted THz power with respect to the total generated power is as low as 6.5%. Given the recorded 1.9 *mW* output power in Ref. 80, the total generated power in that device is estimated to be ~30 *mW*, as shown in Fig. 42(e). There is great potential for THz power enhancement when an efficient THz outcoupler is applied to the THz devices.

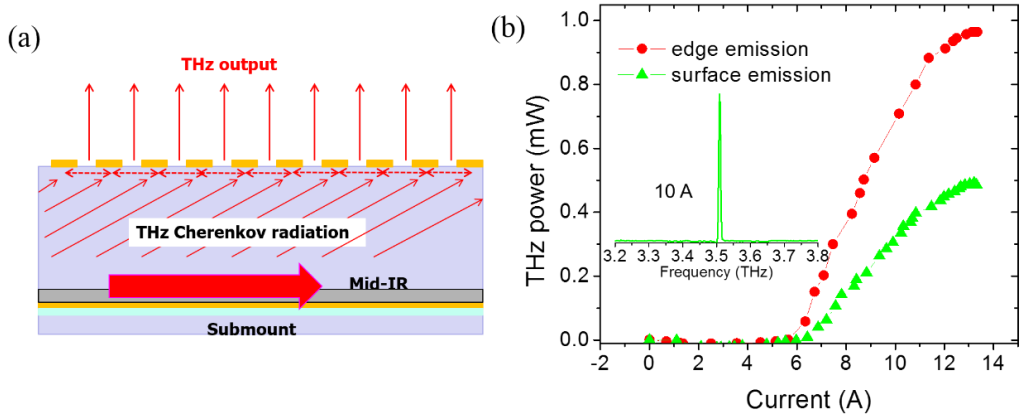

Fig. 43 (a) Schematic of surface emitting diffraction grating for THz. (b) THz power as a function of currents via surface emission and edge emission. Inset: lasing spectra at 10 *A*. Adapted from Ref. [164].

To enhance the THz outcoupling efficiency, a surface-emission scheme based on THz diffraction grating can be defined in the semi-insulating InP substrate of a THz DFG QCL for high-power and efficient THz outcoupling, as shown in Fig. 43(a). Unlike the distributed-feedback (DFB) grating which interacts with the guiding laser mode by providing the optical feedback to the mode, the

THz diffraction grating proposed here simply diffract the incident Čerenkov emission cone into the vertical direction. Here, we report the first THz surface emission via a first-order diffraction grating patterned on the substrate with a demonstrated THz power up to 0.5 *mW*.

The QCL structure is similar to the above THz DFG wafers. The wafer is processed into double-channel waveguide with a ridge width of 20 μm. The 1.5 *mm* long composite DFB section is patterned with a dual period grating within a 3 *mm* long laser cavity. The grating is defined on the InP cap layer with a depth of 0.2 μm. The substrate is then polished and is patterned with a first-order diffraction grating by lift-off Ti/Au (10/1500 *nm*) processing, as shown in Fig. 43(a). The grating period Λ_g is defined by $\Lambda_g = \frac{m\lambda_{THz}}{n_{InP}\cos\theta_c}$, here λ_{THz} is the THz wavelength, n_{InP} is the InP substrate refractive index in THz wavelength range, and m=1, 2, 3, … is the diffraction order. For this work, first-order diffraction grating was designed, with m=1.

The THz output power from surface and edge emission in pulsed mode operation with 1% duty cycle was measured using a calibrated Golay cell detector. The THz spectra were taken in rapid scan mode at a resolution of 0.125 cm^{-1} from a Bruker Fourier transform infrared (FTIR) spectrometer equipped with a far-infrared DTGS detector. The initial THz power characterizations of the epi-down bonded devices are shown in Fig. 43(b). The device emits up to 0.5 *mW* from the surface. Single mode operation at 3.5 *THz* with side mode suppression ratio up to 27 *dB* is achieved (inset of Fig. 43(b)). To examine how much power is emitted from the edge, the substrate near the front facet is polished at 25° with respect to the normal cleavage plane. After polishing, the device emits up to 1.0 *mW*, as shown in Fig. 43(b). The lower surface emission compared to the edge emission is attributed the relatively weak outcoupling efficiency of the metallic diffraction grating. The simulation indicates that only 15% of the generated THz light is outcoupled via the grating.

With further optimization to the diffraction efficiency, such as furthering thinning the InP substrate, or replace the lossy InP substrate with high-resistivity Si substrate, to harvest the THz emission from the entire cavity with an enhanced outcoupling efficiency, high THz power up to 50 *mW* is expected at room temperature for a single laser chip.

In conclusion, we have demonstrated the highest THz peak power up to 1.9 *mW* and CW power of 0.014 *mW* for THz sources based on DFG QCLs at room temperature with a good beam quality and purified spectrum. Room temperature monolithic THz tuning of 2.06-4.35 *THz* at continuous wave operation has also been demonstrated. The rapid development of these types of room temperature devices with compact size will greatly boost the development of THz imaging, sensing, spectroscopy, and many other THz applications.

Quantum cascade laser frequency comb

Quantum cascade laser (QCL) frequency combs have been demonstrated as promising semiconductor frequency comb sources in the mid-IR and THz realm in the past few years [167,

168, 169, 170]. Since the frequency comb is directly generated inside the QCL without any extra optical components, QCL frequency combs are monolithic and chip-based comb sources offering great promise for high-speed, high-resolution spectroscopy. Mid-IR and THz spectroscopy experiments using QCL frequency combs have also been recently demonstrated with high precision and low noise [171, 172]. Higher power and uniform power distribution among the comb modes will always benefit the applications with less scanning time and higher sensitivity.

A highly efficient strain-balanced active region was designed with broadband gain and low dispersion for high comb power operation. The QCL structure is based on a dual-core active region structure with a strong-coupled strain-balanced single-phonon resonance (SPR) designs at λ~7.5 and 8.5 μm [173]. The strong-coupled SPR design not only increases the gain bandwidth and quantum efficiency, but also possesses large nonlinear susceptibilities for four-wave mixing.

High CW power operation at room temperature was obtained for a 4 *mm* long high-reflection (HR) coated comb device as the optical power-current-voltage (*P-I-V*) characterization shown in Fig. 44(b). This device emits a CW power up to 880 *mW* with a threshold current density of 2.05 kA/cm^2. The WPE and slope efficiency are 6.5% and 1.7 *W/A* in CW operation at room temperature (Fig. 44(b)). This is compared with the WPEs less than 1% from previous QCL frequency comb demonstrations [166, 168, 174]. Clearly the device exhibits a broad lasing spectrum at the higher currents with coverage up to 110 cm^{-1}, as shown in the Fig. 44(a). The power distribution is much more uniform that the previous demonstration [168], with over 1 *mW* power for 77% of all the modes, and a high average power-per-mode of about 3 *mW*.

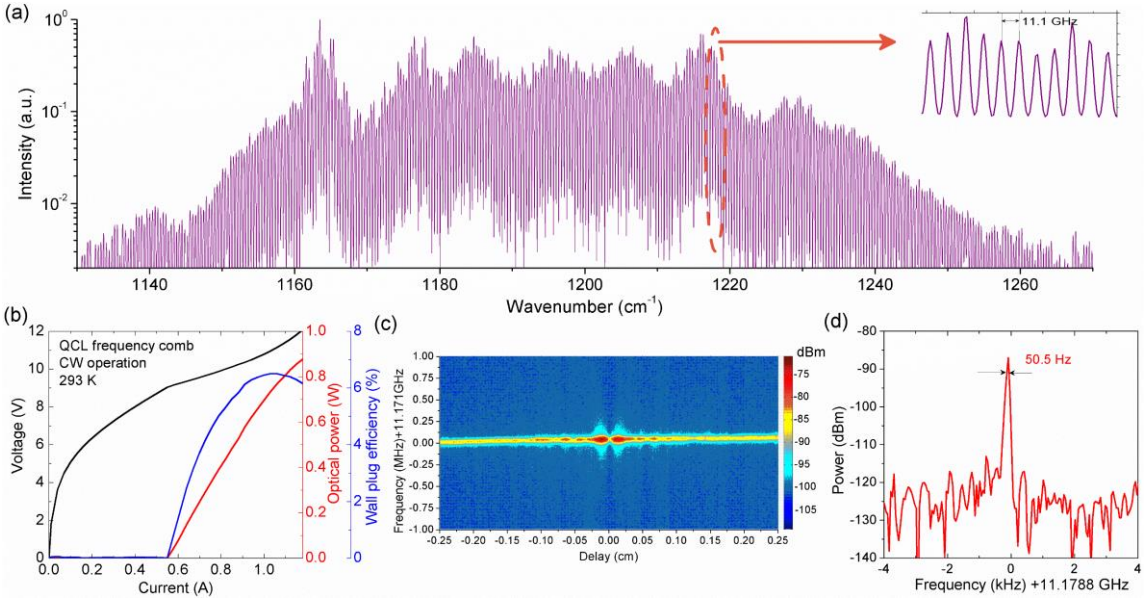

Fig. 44 (a) QCL comb spectrum at a current of 1.06 *A*. The inset is a section of zoomed in spectrum. (b) *P-I-V* characterization of a QCL comb device in CW operation at 20°C. (c) Intermode beat spectroscopy of QCL comb at 938 *mA*.(d) Intermode beatnote spectrum measured at currents of 800 with x=11.18096 *GHz*.

To assess frequency comb operation via phase locking of adjacent laser modes, the linewidth of the intermode beating was measured at the round-trip frequency with a high-speed quantum well infrared detector (QWIP) and a spectrum analyzer (Agilent-E4407B). Extremely narrow beatnote linewidth of 50.5 at 11.1788 *GHz* was observed at 800 mA by using a high resolution scan with RBW=30 *Hz* and span range of 100 *kHz*, as shown in Fig. 44(d). This narrow linewidth reflects that a well-defined phase is established among the frequency comb modes. At higher currents of ≥1083 *mA*, the beatnote spectrum broadens to 400 *kHz* with a flat top, which indicates the QCL comb device operates in the high-phase-noise regime. The group delay dispersion (GDD) measurement for this device reveals that the high-phase-noise regime is attributed to the residual GDD inside the laser cavity. The intermode beat spectroscopy in Fig. 44(c) indicates that the entire lasing spectrum at a current of 938 *mA* contributed to the comb operation.

The net positive dispersion presented in the cavity can be largely diminished by using a Gires–Tournois interferometers (GTI) mirror based dispersion compensation technique. Recently, GTI mirror based on Y_2O_3/TiO_2 with nominal optical absorption was designed and directly deposited on the back facet using ion-beam deposition (IBD) system for dispersion compensation [175], as shown in Fig. 45(a). The layer thicknesses of the multi-layer dielectrics are: 660/**200**/660/**200**/660/**200**/660/**200**/660/**200**/660. TiO_2 layers are in bold font. The GTI coating was terminated with a 120-*nm* Au layer using e-beam evaporation system. A reflectivity spectrum for the GTI mirror deposited on the InP substrate sample was acquired by using a Globar as the mid-IR source, as plotted in (a). High reflectivity of 92% for wavelength at 8 μm was obtained, and above 85% for long wavelength up to 10 μm. This implies that GTI mirror using Y_2O_3 and TiO_2 is able to provide high reflectivity for the entire 3–10 μm wavelength range. GDD of this structure was evaluated through the invert Fourier transform to the first burst of the reflectivity interferogram, as depicted in Fig. 45(b). A theoretical calculation of the GDD spectrum based on a transfer matrix method was performed. As shown in Fig. 45(b), the calculated dispersion matches well with the experimental data. Negative dispersion of -4500 fs^2 at 1250 cm^{-1} was measured which is sufficient to compensate the dispersion residue in the comb device.

A 4.03 *mm* long device was coated with Y_2O_3/TiO_2 GTI mirror on the back facet and epi-down mounted on a diamond for testing. The measured relative phase $\Delta\varphi$ spectrum in Fig. 45(a) presents an opposite sign with a much milder change compared to that of a HR-coated device. As a result, the GTI coated comb device exhibits a near zero dispersion in the lasing spectral range near threshold currents. The group delay dispersion was largely decreased to below zero in the lasing spectral range, which will be beneficial for frequency comb operation.

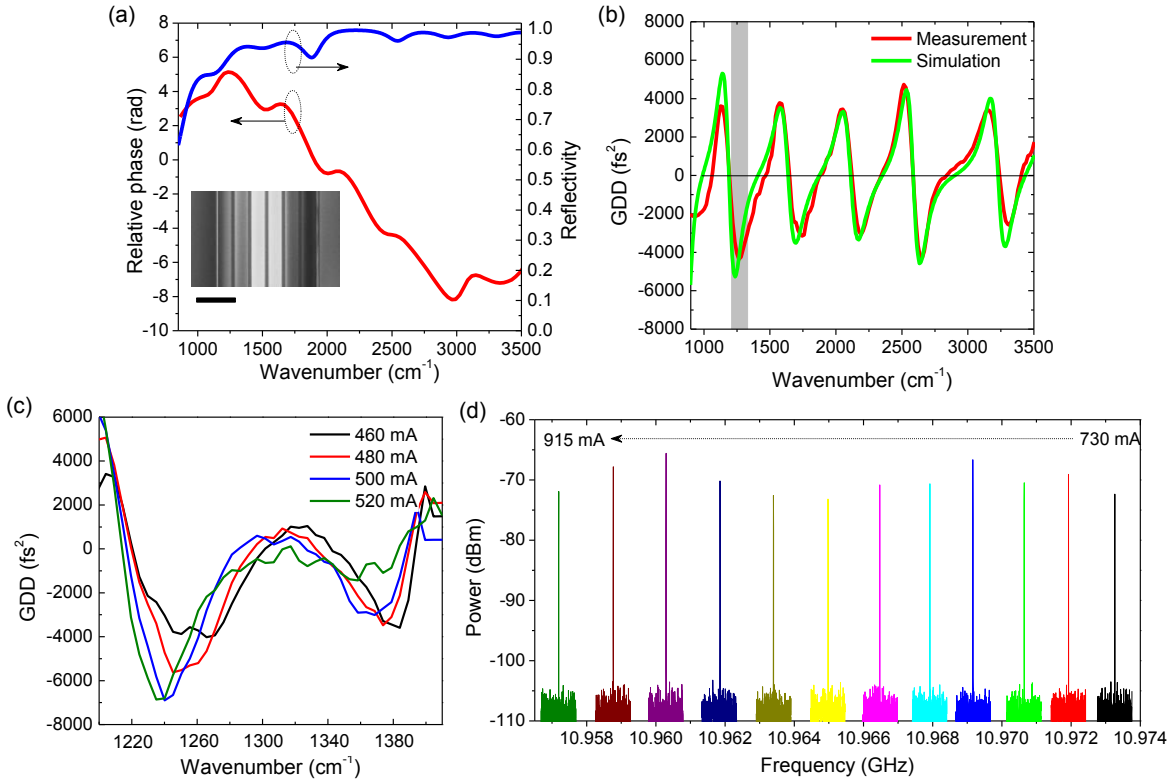

Fig. 45 (a) Reflectivity and relative phase spectra of the GTI mirror. Inset: SEM image of the GTI mirror. (b) Measured and calculated GDD spectra of the GTI mirror. (c) Measured GDD of a GTI-mirror-coated QCL comb at different currents. (d) Beatnote spectra as functions of currents from 730 *mA* to 915 *mA*. Adapted from Ref. [175].

The RF beatnote spectra for comb operation were recorded via a QWIP detector and spectrum analyzer. After the current 730 *mA*, narrow beatnote spectra with SNR greater than 35 *dB* were measured up to roll-over currents, and no high-phase noise regime was observed, as shown in Fig. 45(d). The beatnote spectra were acquired with a span range of 1 *MHz* and resolution bandwidth (RBW) of 300 *Hz* for all the currents. The linewidth stays fairly narrow and constant, FWHM~700 *Hz* for the current of 730 *mA* near the comb threshold and FWHM~800 *Hz* for the current 905 *mA* near the roll-over. Note that the beatnote linewidth is mainly limited by the RBW. A high resolution scan with RBW=30 *Hz* spanning 10 *kHz* was performed, and a narrow beatnote linewidth of 40 *Hz* was observed at a current of 869 *mA*. Compared with the normal HR coated device with uncontrollable beatnote linewidths, this is because that the compensated dispersion of the GTI-coated cavity enhances the mode locking efficiency via four wave mixing process.

The rapid development of monolithic high power efficiency QCL frequency comb source with a wide spectral coverage will find wide applications especially in high-precision remote spectroscopy and sensing, and lead to the THz frequency comb generation at room temperature based on intracavity difference-frequency generation in QCLs [80, 149].

Tab. III Quantum cascade laser accomplishments in CQD being integral to the development of high power THz sources. Boldface year indicates current world record.

Year	Accomplishment	Reference
1997	First QCL growth by Gas-MBE.	128
2001	High temperature (T>425 K) operation of ~11 m QCL.	176
2003	First CW QCL (~6 m) at room temperature.	177
2005	First room temperature CW single mode QCL at ~4.8 m.	178
2006	Longest wavelength (= 11.5 m) CW QCL at room temperature.	130
2008	Demonstration of Watt-level CW QCL at room temperature.	179
2009	Highest peak power QCL (120 W).	180
2010	Highest efficiency QCLs in the world (53% @ 40 K, 27% at 300 K).	132
2010	Highest peak power, single mode QCL (34 W).	136
2011	Highest CW power, single mode QCL (2.4 W).	135
2011	Highest power CW surface-emitting ring laser.	143
2011	Highest power (5 W) and efficiency (21%) room temperature CW QCL.	131
2012	Shortest wavelength (= 3 m) CW QCL at room temperature.	129
2013	Widest electrical tuning (243 cm^{-1}) for a single mode quantum cascade laser.	138
2014	Broadest gain bandwidth (4–12 m wavelength) with multi-core heterogeneous QCL.	unpublished
2014	First CW and highest peak power (1.9 mW) QCL-based THz sources at room temperature.	157
2014	Widest monolithically tunable THz sources (2.8–4.2 THz) at room temperature.	166
2015	First monolithic solid state frequency comb (130 cm^{-1} span) at ~ 9 m.	169
2015	Highest peak power (203 W) semiconductor laser with near diffraction-limited beam quality	133
2015	Highest CW power (>1 W) and peak power (5 W) tunable QCLs.	142
2016	First monolithic laser array tunable from 6.2–9.1 m with beam combiner.	141
2017	Highest power (0.88 W) solid state frequency comb (110 cm^{-1} span).	173
2017	Widest monolithic beam steering (17.9^{o}) based on a grating outcoupler.	142
2017	Highest efficiency (20.5%) long wavelength (= 8.3 m) QCL	unpublished

Conclusion

In conclusion, the THz spectral region is of significant interest to the scientific community, but is one of the hardest regions to access with conventional technology. A number of application areas are currently being developed in this spectral region related to spectroscopy, imaging, medical and biological sciences, environmental monitoring, security and defense, astronomy, condensed matter research, plasma diagnostics, and communications. These opportunities are initiating a new revolution in THz technology, especially with regard to the development of compact and versatile devices for THz emission and detection based on semiconductor optoelectronics.

The next generation of THz technology will draw from technological advances made in a variety of semiconductor material systems. This includes the III-Nitride material system which exhibits the potential for both high speed electronic and intersubband optical devices thanks to a wide tunable direct bandgap, large longitudinal optical phonon energies, inherit fast carrier dynamics, good carrier transport properties, high breakdown fields, and high robustness and chemical stability.

The GaAs-based system was also explored, which was developed for both high power lasers and intersubband devices. There has also been rapid development in this system for devices in the THz spectral region. However, a shift from Al-based to Al-free alloys was presented as a future direction that is worth exploring for improving device performance.

The last set of materials, based on InP, GaInAs(P), and AlInAs has seen a number of revolutionary advances which are relevant to THz technology. Drawing from initial optimization of GaInAsP alloys for telecommunications application, this system was later developed for a wide variety of intersubband devices, including QWIPs and QCLs. While direct access to the THz spectral region has been demonstrated with these materials, these devices still tend to require cryogenic cooling to operate. New architectures, such as the QDIP and QCLs with integrated nonlinearities, are presented as ways to combat this temperature limitation. The DFG QCL has already demonstrated high power (mW-level) room temperature emission of THz radiation over a wide spectral range. Some opportunities to improve the nonlinear conversion efficiency and optimize power extraction are explored as future directions. In addition, by utilizing both second-order- and third-order nonlinearities in the QCL, it is also proposed that room temperature THz frequency combs may soon be achievable.

Taken all together, there are many exciting new semiconductor optoelectronic technologies that are coming together to close the 'THz gap'. These future devices promise easy access and low costs, building on demonstrated high temperature operation and wafer scale manufacturing. There is truly a bright future for THz technology.

References

[1] http://www.nepanh.org/emf.html

[2] B. S. Alexandrov, V. Gelev, A. R. Bishop, et al. "DNA breathing dynamics in the presence of a terahertz field". *Physics Letters A*, 374, 1214 (2010)

[3] A. Korenstein-Ilan, A. Barbul, P Hasin, et al. "Terahertz Radiation Increases Genomic Instability in Human Lymphocytes". *Rad. Res*. 170, 224 (2008).

[4] A. Homenko, B. Kapilevich, R. Kornstein, et al. "Effects of 100 GHz radiation on alkaline phosphatase activity and antigen-antibody interaction". *Bioelectromagnetics*, 30, 167 (2009).

[5] N. P. Bondar, I. L. Kovalenko, D. F. Avgustinovich, et al. "Behavioral effect of terahertz waves in male mice". *Bull. Exp. Biol. Med*., 145, 4 (2008).

[6] Y. -S. Lee. "Principles of Terahertz Science and Technology". *Springer* (2008).

[7] R. A. Lewis. "A review of THz sources". *J. Phys. D: Appl. Phys.* 47, 374001 (2014)

[8] M. Yamashita, K. Kawase, C. Otani, et al.. in Conf. Optical Terahertz Science and Technology doc ID: TuC4 Florida, USA (2005).

[9] H. Zhong, J. Xu, X. Xie, et al. "Nondestructive defect identification with terahertz time-of-flight tomography". *IEEE Sensors J*., 5, 203–208 (2005).

[10] Y. B. Ji, E. S. Lee, S. -H. Kim, et al. "A miniaturized fiber-coupled terahertz endoscope system". *Optics Express*, 17, 17082 (2009).

[11] J. W. Waters, L. Froidevaux, R. S. Harwood, et al. "The earth observing system microwave limb sounder (EOS MLS) on the aura satellite". *IEEE Trans. Geosci. Remote Sensing*, 44, 1075–1092 (2006)

[12] R. A. Cheville and D. Grischkowsky. "Time domain terahertz impulse ranging studies". *Appl. Phys. Lett*., 67(14):1960–1962 (1995).

[13] R. A. Cheville, R.W. McGowan, and D.R. Grischkowsky. "Latetime target response measured with terahertz impulse ranging". *IEEE Transactions on Antennas and Propagation*, 45(10), 1518–1524 (1997).

[14] X. J. Zhong, T. J. Cui, Z. Li, et al. "Terahertz-wave scattering by perfectly electrical conducting objects". *J. Electromagnet. Wave*, 21(15), 2331–2340 (2007).

[15] J. Pearce and D. M Mittleman. "Scale model experimentation: using terahertz pulses to study light scattering". *Physics in Medicine and Biology*, 47(21), 3823 (2002).

[16] C. K. Walker. "THz Astronomy". *CRC Press* (2015).

[17] P. U. Jepsen, D. G. Cooke and M. Koch. "Terahertz spectroscopy and imaging - modern techniques and applications". *Laser Phot. Rev*. 5 (1), 124 (2011).

[18] D. C. Larrabee, G. A. Khodaparast, F. K. Tittel, et al. "Application of THz QCLs to semiconductor cyclotron resonance". *Optics Lett*., 29 (1), 122 (2004).

[19] D. N. Basov, R.D. Averitt, D. van der Marel, et al. "Electrodynamics of correlated electron materials". *Rev. Mod. Phys*., 83 (2), 471 (2011).

[20] D. Wiersma. "Laser physics: the smallest random laser". *Nature*, 406, 132–133 (2000).

[21] M. Koch, "Terahertz Communications: A 2020 vision". Nato Science for Peace and Security Series—B: Physics and Biophysics, edited by R. E. Miles, X. C. Zhang, H. Eisele, and A. Krotkus, Springer Science and Business Media, Dordrecht, Netherlands, 325–338 (2007).

[22] D. C. O'Brien, G.E. Faulkner, K. Jim, et al.. "High-speed integrated transceivers for optical wireless". *IEEE Communications Magazine*, 41(3)3, 58–62 (2003).

[23] V. Jungnickel, T. Haustein, A. Forck, et al. "155 Mbit/s wireless transmission with imaging infrared receiver". *IEEE Electronics Letters*, 37(5), 314–315 (2001).

[24] M. Wolf and D. Kress. "Short-Range Wireless infrared transmission: the link budgetcompared to RF". *IEEE Wireless Communications*, 10(2), 8–14 (2003).

[25] M. Fujishima, S. Amakawa, K. Takano, et al. "Terahertz CMOS design for low-power and high-speed wireless communication". *IEICE Trans. Electron*., E98-C, 1091–1104 (2015).

[26] T. Nagatsuma, G. Ducournau and C. C. Renaud. "Advances in terahertz communications accelerated by photonics". *Nature Photonics*, 10, 371-379 (2016).

[27] K. Balakier, M. J. Fice, F. V. Dijk, et al. "Optical injection locking of monolithically integrated photonic source for generation of high purity signals above 100 GHz". *Opt. Express*, 22, 29404–29412 (2014).

[28] H. J. Song, K. Ajito, Y. Muramoto, et al. "Uni-travelling-carrier photodiode module generating 300 GHz power greater than 1 mW". *IEEE Microw. Wireless Components Lett*., 22, 363–365 (2012).

[29] F. V. Dijk, G. Kervella, M. Lamponi, et al. "Integrated InP heterodyne millimeter wave transmitter". *IEEE Photon. Technol. Lett*., 26, 965–968 (2014).

[30] M. J. R. Heck, J. F. Bauters, M. L. Davenport, et al. "Hybrid silicon photonic integrated circuit technology". *IEEE J. Sel. Top. Quant. Electron*, 19, 6100117 (2013).

[31] G. H. Duan, C. Jany, A. L. Liepvre, et al. "Hybrid III-V on silicon lasers for photonic integrated circuits on silicon". *IEEE J. Sel. Top. Quant. Electron*., 20, 6100213 (2014).

[32] A. Saxler, P. Kung, C.J. Sun, et al. "High Quality Aluminum Nitride Epitaxial Layers Grown on Sapphire Substrates". *Appl. Phys. Lett*., 64, 339 (1994).

[33] C. J. Sun, P. Kung, A. Saxler, et al. "A Crystallographic Model of (00*1) Aluminum Nitride Epitaxial Thin Film Growth on (00*1) Sapphire Substrate". *J. Appl. Phys.*, 75, 3964 (1994).

[34] M. Razeghi and M. Henini. "Optoelectronic Devices: III-Nitrides". *Elsevier, Gulf Professional Publishing*, 1st edition (2004).

[35] F. S. Johnson. "Solar Radiation: Space Materials Handbook". edited by G. G. Claus and B. S. J. Singletary (Lookheed Missiles and Space Co.,Sunnyvale, January 1962), pp. 31–37.

[36] M. Razeghi. "Short Wavelength Solar-Blind Detectors: Status, Prospects, and Markets". *Proc. IEEE*, 90, 1006 (2002).

[37] P. Kung, A. Yasan, R. McClintock, et al. "Future of $Al_xGa_{1-x}N$ Materials and Device Technology for Ultraviolet Photodetectors". *Proc. SPIE*, 4650, 199 (2002).

[38] E. Cicek, R. McClintock, C. Y. Cho, et al. "$Al_xGa_{1-x}N$-based back-illuminated solar-blind photodetectors with external quantum efficiency of 89%". *App. Phys. Lett*., 103, 191108 (2013)

[39] R. McClintock, A. Yasan, K. Mayes, et al. "Back-illuminated solar-blind photodetectors for imaging applications". *Proc. SPIE*, 5732, 175 (2005)

[40] P. Kung, A Yasan, R. McClintock, et al. "Future of $Al_xGa_{1-x}N$ materials and device technology for ultraviolet photodetectors". *Proc. SPIE*, 4650, 199-206 (2002).

[41] M. Ulmer, M. Razeghi and E. Bigan. "Ultra-Violet Detectors for Astrophysics, Present and Future". *Proc. SPIE*, 2397, 210-216 (1995).

[42] I. J. Oguzman, E. Bellotti, K. Brennan, et al. "Theory of hole initiated impact ionization in bulk zincblende and wurtzite GaN". J. Appl. Phys., 81, 7827 (1997).

[43] R. McClintock, J. L. Pau, K. Minder, et al. "Hole-initiated multiplication in back-illuminated GaN avalanche photodiodes". *Appl. Phys. Lett*., 90, 141112 (2007).

[44] J. L. Pau, C. Bayram, R. McClintock, M. Razeghi, et al. "Back-illuminated separate absorption and multiplication GaN avalanche photodiodes". *Appl. Phys. Lett.*, 92, 101120 (2008).

[45] S. Nakamura, M. Senoh, S. -I. Nagahama, et al. "InGaN-Based Multi-Quantum-Well-Structure Laser Diodes". *Jpn. J. Appl. Phys.*, 35, L74–L76 (1996).

[46] S. Nakamura, M. Senoh, S. Nagahama, et al. "Room-temperature continuous-wave operation of InGaN multi-quantum-well structure laser diodes". *Appl. Phys. Lett*., 69, 4056–4058 (1996).

[47] P. Kung, A. Saxler, D. Walker, et al. "AlGaN-based materials and heterostructures". *Mat. Res. Soc. Symp*. *Proc*., 449, 79-84 (1997).

[48] M. Razeghi, A. Saxler, P. Kung, et al. "Continuous-wave room-temperature operation of InGaN/GaN multiquantum well lasers grown by low-pressure metalorganic chemical vapor deposition". *Proc. SPIE*, 3284, 113-121 (1998).

[49] K. Mayes, A. Yasan, R. McClintock, et al. "High Power 280 nm AlGaN Light Emitting Diodes Based on an Asymmetric Single Quantum Well". *Appl. Phys. Lett*., 84, 1046 (2004).

[50] A. Yasan, R. McClintock, K. Mayes, et al. "4.5 mW Operation of AlGaN-based 267 nm Deep-Ultraviolet Light-Emitting Diodes". *Appl. Phys. Lett*., 83, 4701 (2003).

[51] C. -Y. Cho, Y. Zhang, E. Cicek, et al. "Surface plasmon enhanced light emission from AlGaN-based ultraviolet light-emitting diodes grown on Si (111) ". *Appl. Phys. Lett*., 102, 211110 (2013).

[52] P. Kung, A. Saxler, D. Walker, et al. "GaInN/GaN Multi-Quantum Well Laser Diodes Grown by Low-Pressure Metalorganic Chemical Vapor Deposition". *MRS Internet J. Nitride Semicond*. Res., 3, 1 (1998).

[53] E. Cicek, R. McClintock, C. Y. Cho, et al. "$Al_xGa_{1-x}N$-based solar-blind ultraviolet photodetector based on lateral epitaxial overgrowth of AlN on Si substrate". *Appl. Phys. Lett*., 103, 181113 (2013).

[54] Y. Zhang, S. Gautier, C. Cho, et al. "Near milliwatt power AlGaN-based ultraviolet light emitting diodes based on lateral epitaxial overgrowth of AlN on Si(111)". *Appl. Phys. Lett*., 102(1), 011106-1 (2013).

[55] Z. Vashaei, C. Bayram, R. McClintock, et al. "Effects of substrate quality and orientation on the characteristics of III-nitride resonant tunneling diodes". *Proc. SPIE*, 7945, 79451A (2011).

[56] C. Bayram, Z. Vashaei and M. Razeghi. "Reliability in room-temperature negative differential resistance characteristics of low-aluminum contact AlGaN/GaN double-barrier resonant tunneling diodes". *Appl. Phys. Lett.*, 97(18), 181109-1 (2010).

[57] M. Razeghi. "The MOCVD Challenge: A survey of GaInAsP-InP and GaInAsP-GaAs for photonic and electronic device applications". *Second Edition, Taylor and Francis/CRC Press, Boca Raton, FL* (2011)

[58] M. Razeghi, M. Defour, F. Omnes, et al. "Extremely High Electron Mobility in a GaAs-GaInP Heterostructure Grown by MOCVD". *Appl. Phys. Lett.*, 55, 457 (1989).

[59] M. Razeghi, M. Maurel, F. Omnes, et al. "First Observation of the Two-Dimensional Properties of the Electron Gas in GaInP/GaAs Heterojunctions Grown by Low-Pressure Metalorganic Chemical Vapor Deposition". *Appl. Phys. Lett.*, 48, 1267-1269 (1986).

[60] M. Razeghi. Patent on "0.808 μm InGaAsP/ GaAs lasers for Nd:YAG pumping". Patent No. 56032, Thompson C.S.F. France (1988).

[61] M. Razeghi. Patent on "optoelectronic devices based on GaAs/ Ga1-xInxAs/ Ga1-xInxAsyP1-y". Patent No. 57666, Thompson C.S.F. France (1990)

[62] M. Razeghi. "High-power laser diodes based on InGaAsP alloys". *Nature*, 369, 631-633(1994).

[63] H. Yi, J. Diaz, L. J. Wang, et al. "Optimized structure for InGaAsP/GaAs 808 nm high power lasers". *Appl. Phys. Lett*., 66, 3251-3253 (1995).

[64] K. Mobarhan, M. Razeghi, G. Marquebielle, et al. "High-Power, 0.98 μm, $Ga_{0.8}In_{0.2}As/GaAs/Ga_{0.51}In_{0.49}P$ Multiple Quantum-Well Laser". *J. Appl. Phys*., 72, 4447-4448 (1992).

[65] J. Diaz, H. J. Yi, S. Kim, et al. "High Temperature Reliability of Aluminum-free 980 nm and 808 nm Laser Diodes". Compound Semiconductors 1995, in: J.-C. Woo and Y. S. Park (Eds.), Institute of Physics Conference Series no.145, Institute of Physics Publishing, Bristol, pp. 1041-1046 (1996).

[66] J. Diaz, H. J. Yi and M. Razeghi. "Long-term reliability of Al-free InGaAsP/GaAs (λ = 808nm) lasers at high-power high-temperature operation". *Appl. Phys. Lett.*, 71, 3042-3044 (1997).

[67] M. Razeghi. "Aluminum Free 650 nm to 1100 nm High Power Lasers grown on GaAs, InP and Si Substrates". US Patent 5389396 (1995).

[68] J. Hoff, S. Kim, M. Erdtmann, et al. "Background Limited Performance in p-doped $GaAs/Ga_{0.71}In_{0.29}As_{0.39}P_{0.61}$ Quantum Well Infrared Photodetectors". *Appl. Phys. Lett.*, 67, 22 (1995).

[69] J. R. Hoff, M. Razeghi and G. Brown. "Effect of the spin split-off band on optical absorption in p-type $Ga_{1-x}In_xAs_yP_{1-y}$ quantum-well infrared detectors". *Phys. Rev.* B, 54, 10773, (1996).

[70] C. Jelen, S. Slivken, J. Hoff, et al. "Aluminum free GaInP/GaAs Quantum Well Infrared Photodetectors for Long Wavelength Detection". *Appl. Phys. Lett.*, 70, 360 (1997).

[71] S. Kim, H. Mohseni, M. Erdtmann, et al. "Growth and characterization of InGaAs/InGaP quantum dots for mid-infrared photoconductive detector". *Appl. Phys. Lett.*, 73, 963 (1998).

[72] J. Jiang, K. Mi, S. Tsao, et al. "Demonstration of a 256x256 Middle-Wavelength Infrared Focal Plane Array based on InGaAs/InGaP Quantum Dot Infrared Photodetectors (QDIPs)". *Appl. Phys. Lett.* 84, 2232, (2004).

[73] R. Köhler, A. Tredicucci, F. Beltram, et al. "Terahertz Semiconductor-Heterostructure Laser". *Nature*, 417, 156−159 (2002).

[74] P. Bhattacharya. "The relationship of the D-X centre in $Al_xGa_{1-x}As$ and other III-V alloys with the conduction band structure". *Semicond. Sci. Technol.*, 3, 1145 (1988).

[75] L. Ajili, G. Scalari, N. Hoyler, et al. "InGaAs−AlInAs/InP Terahertz Quantum Cascade Laser". *Appl. Phys. Lett.*, 87, 141107 (2005).

[76] K. Ohtani, M. Beck, G. Scalari, et al. "Terahertz Quantum Cascade Lasers Based on Quaternary AlInGaAs Barriers". *Appl. Phys. Lett.*, 103, 041103 (2013).

[77] C. Deutsch, A. Benz, H. Detz, et al. "Terahertz Quantum Cascade Lasers Based on Type II InGaAs/ GaAsSb/InP". *Appl. Phys. Lett.*, 97, 261110 (2010).

[78] M. Brandstetter, M. A. Kainz, T. Zederbauer, et al. "InAs Based Terahertz Quantum Cascade Lasers". *Appl. Phys. Lett.*, 108, 011109 (2016).

[79] M. Fischer, G. Scalari, K. Celebi, et al. "Scattering Processes in Terahertz InGaAs/InAlAs Quantum Cascade Lasers". *Appl. Phys. Lett*., 97, 221114 (2010).

[80] M. Razeghi, Q. Y. Lu, N. Bandyopadhyay, et al. "Quantum cascade lasers: from tool to product". *Opt. Express*, 23, 8462 (2015).

[81] C. Deutsch, H. Detz, M. Krall, et al. "Dopant Migration Effects in Terahertz Quantum Cascade Lasers". *Appl. Phys. Lett.*, 102, 201102 (2013).

[82] M. Razeghi, M. Defour, F. Omnes, et al. "Extremely high electron mobility in a GaAs - $Ga_xIn_{1-x}P$ heterostructure grown by metalorganic chemical vapor deposition". *Appl. Phys. Lett.*, 55, 457, (1989).

[83] M. Razeghi, F. Omnes, M. Defour, et al. "High performance GaAs/GaInP heterostructure bipolar transistors grown by low-pressure metal-organic chemical vapour deposition". *Semicond. Sci. Technol*., 5, 278-280 (1990).

[84] S. L. Feng, J. Krynicki, V. Donchev, et al. "Band offset of GaAs-GaInP heterojunctions". *Semicond. Sci. Technol.*, 8, 2092-2096 (1993).

[85] E. Michel, G. Singh, S. Slivken, et al. "Molecular Beam Epitaxial Growth of High Quality InSb". *Appl. Phys. Lett.*, 65, 3338 (1994).

[86] G. Singh, E. Michel, C. Jelen, et al. "Molecular Beam Epitaxial Growth of High Quality InSb for p-i-n Photodetectors". *J. Vac. Sc. Technol.* B, 13, 782 (1995)

[87] E. Michel, J. Xu, J.D. Kim, et al. "InSb Infrared Photodetectors on Si Substrates Grown by Molecular Beam Epitaxy". *IEEE Photonics Technol. Lett.*, 8, 673 (1996)

[88] E. Michel, H. Mohseni, J. Wojkowski, et al. "InSb Detectors and Focal Plane Arrays on GaAs, Si, and Al_2O_3 Substrates". *Materials Research Society Symposium*, Dec. 2 (1996)

[89] E. Michel, J.D. Kim, S. Park, et al. "Sb-based infrared materials and photodetectors for the 3-5 and 8-12 μm range". SPIE Photonics West '96' Photodetectors: Materials and Devices'; *Proceedings* 2685, Jan. 27 (1996)

[90] J. D. Kim, S. Kim, D. Wu, et al. "8-13 μm InAsSb heterojunction photodiode operating at near room temperature". *Appl. Phys. Lett.*, 67, 2645 (1995).

[91] J. D. Kim, D. Wu, J. Wojkowski, et al. "Long-Wavelength InAsSb Photoconductors Operated at Near Room Temperatures (200-300 K)". *Appl. Phys. Lett.*, 68, 99 (1996).

[92] J. S. Wojkowski, H. Mohseni, J. D. Kim, et al. "Demonstration of InAsSb/AlInSb Double Heterostructure Detectors for Room Temperature Operation in the 5–8 μm Wavelength Range". *Proc. SPIE, San Jose, CA, Jan*. 27 (1999).

[93] J. D. Kim, H. Mohseni, J. S. Wojkowski, et al. "Growth of InAsSb Alloys on GaAs and Si Substrates for Uncooled Infrared Photodetector Applications". *SPIE Conference, San Jose, CA, Jan.* 27 (1999).

[94] J. J. Lee, J. D. Kim and M. Razeghi. "Growth and characterization of InSbBi for long wavelength infrared photodetectors". *Appl. Phys. Le*tt., 70, 3266 (1997).

[95] J. J. Lee, J. D. Kim and M. Razeghi. "Room temperature operation of 8–12 μm InSbBi infrared photodetectors on GaAs substrates". Appl. Phys. Lett., 73, 602 (1998).

[96] J. J. Lee, J. D. Kim and M. Razeghi, "Exploration of Novel InSbBi Alloy for Uncooled Infrared Photodetector Applications". *Special issue of the Journal of the Korean Physical Society*, 35, July 1 (1999).

[97] M. Razeghi. "Novel Sb-based alloy for uncooled infrared photodetector applications". *Proc. SPIE* 4288, Photodetectors: Materials and Devices VI (12 June 2001); doi: 10.1117/12.429414.

[98] Y. H. Choi, R. Sudharsanan, C. Besikci, et al. "Growth of $In_{1-x}Tl_xSb$, a New Infrared Material, by Low-Pressure Metalorganic Chemical Vapor Deposition". *Appl. Phys. Lett*., 63, 361 (1993).

[99] P. T. Staveteig, Y. H. Choi, G. Labeyrie, et al. "Photoconductance measurements on InTlSb/InSb/GaAs grown by low-pressure metalorganic chemical vapor deposition". *Appl. Phys. Lett.*, 64, 460 (1994).

[100] Y. H. Choi, P. Staveteig, E. Bigan, et al. "Characterization of InTlSb/InSb Grown by Low Pressure Metalorganic Chemical Vapor Deposition on GaAs Substrate". *J. Appl. Phys.*, 75, 3196 (1994).

[101] J. J. Lee, J. D. Kim and M. Razeghi. "Novel InTlSb Alloy for Uncooled Long-Wavelength Infrared Photodetectors". *Opto-Electron. Rev*., 7, 19 (1999).

[102] J. D. Kim, E. Michel, S. Park, et al. "Room-temperature operation of InTlSb infrared photodetectors on GaAs". *Appl. Phys. Lett*. 69, 343 (1996).

[103] http://cqd.eecs.northwestern.edu/research/intlasbisb.php

[104] M. Razeghi, S. Abdollahipour, E. K. Huang, et al. "Type-II InAs/GaSb photodiodes and focal plane arrays aimed at high operating temperatures". *Opto-Electron*. Rev., 19, 261 (2011)

[105] M. Razeghi, A. Haddadi, A.M. Hoang, et al. "Advances in antimonide-based Type-II superlattices for infrared detection and imaging at center for quantum devices". *Infrared Physics & Technology*, 59, 41 (2013)

[106] M. Razeghi. "Focal Plane Arrays in Type-II Superlattices". *US Patent* 6864552, (2005).

[107] H. Mohseni, V. I. Litvinov and M. Razeghi. "Interface-induced suppression of the Auger recombination in Type-II InAs/GaSb superlattices". *Phys. Rev. B, 58*, 15378 (1998).

[108] A. M. Hoang, G. Chen, A. Haddadi, et al. "Demonstration of short wavelength infrared photodiodes based on Type-II InAs/GaSb/AlSb superlattices". *Appl. Phys. Lett*., 100, 211101 (2012).

[109] S. A. Pour, E. K. Huang, G. Chen, et al. "High operating temperature mid-wave infrared photodiodes and focal plane arrays based on Type-II InAs/GaSb superlattices". *Appl. Phys. Lett*., 98, 143501 (2011).

[110] E. K. Huang and M. Razeghi. "World's first demonstration of type-II superlattice dual band 640x512 LWIR focal plane array". *Proc. SPIE*, 8268, 82680Z (2012).

[111] Y. Wei and M. Razeghi. "Modeling of Type-II InAs/GaSb superlattices using an empirical tight-binding method and interface engineering". *Phys. Rev. B*, 085316 (2004).

[112] M. Razeghi, P. Hirtz, R. Blondeau, et al. "Aging Test of MOCVD Shallow Proton Stripe GaInAsP-InP DH Laser Diode Emitting at 1.5 μm". *Electron. Lett.*, 19, 481 (1983).

[113] M. Razeghi, S. Hersee, R. Blondeau, et al. "Very Low Threshold GaInAsP/InP DH Lasers Grown by MOCVD". *Electron. Lett*., 19, 336 (1983).

[114] M. Razeghi, R. Blondeau, M. Krakowski, et al. "Low-Threshold Distributed Feedback Lasers Fabricated on Material Grown Completely by LP-MOCVD". *IEEE J. of Quantum Elect.*, 21, 507-511 (1985).

[115] J. Nagle, S. Hersee, M. Razeghi. "Properties of 2D Quantum-Well Lasers". *Surf. Sci*., 174, 148 (1986).

[116] M. Razeghi. "CW Phase-Locked Array GaInAsP-InP High Power Semiconductor Laser Grown by Low-Pressure Metalorganic Chemical Vapor Deposition". *Appl. Phys. Lett*., 50, 230 (1987).

[117] M. Razeghi, R. Blondeau and J. P. Duchemin. "$Ga_xIn_{1-x}As_yP_{1-y}$ – InP, DH lasers emitting at 1.3 μm grown on GaAs by LP-MOCVD growth technique", in GaAs and Related Compounds 1984, Inst. *Phys. Conf. Ser*. No. 74, p. 679, *Adam Hilger, Bristo*l (1985).

[118] M. Razeghi, M. Defour, F. Omnes, et al. "First GaInAsP-InP Double Heterostructure Laser Emitting at 1.27 μm on a Silicon Substrate". *Appl. Phys. Lett.*, 53, 725 (1988).

[119] M. Razeghi, F. Omnes, R. Blondeau, et al. "A High Quantum Efficiency GaInAs-InP Photodetector on Si Substrate". *J. Appl. Phys*., 65, 4066 (1989).

[120] C. Jelen, S. Slivken, T. David, et al. "Responsivity and Noise Performance of InGaAs/InP Quantum Well Infrared Photodetectors". *Proc. SPIE*, 3287, 96 (1998).

[121] C. Jelen, S. Slivken, V. Guzman, et al. "InGaAlAs–InP Quantum-Well Infrared Photodetectors for 8–20 μm Wavelengths". *IEEE J. Quant. Elect.*, 34, 1873 (1998).

[122] C. Jelen, S. Slivken, G. J. Brown, et al. "Multi-color 4–20 μm In-P-based Quantum Well Infrared Photodetectors". *Proc. SPIE*, 3629, 147 (1999).

[123] J. Jiang, K. Mi, R. McClintock, et al. "Demonstration of 256x256 Focal Plane Arrays Based on Al-free GaInAs/InP QWIP". *IEEE Phot. Technol. Lett.*, 15, 1273 (2003).

[124] J. Jiang, C. Jelen, M. Razeghi, et al. "High Detectivity GaInAs–InP Quantum-Well Infrared Photodetectors Grown on Si Substrates". *IEEE Photon. Technol. Lett*., 14, 372 (2002).

[125] H. Lim, S.Tsao, W. Zhang, et al. "High-performance InAs quantum-dot infrared photodetectors grown on InP substrate operating at room temperature". *Appl. Phys. Lett*., 90, 131112 (2007).

[126] S. Tsao, H. Lim, W. Zhang, et al. "High operating temperature 320x256 middle-wavelength infrared focal plane array imaging based on an InAs/InGaAs/InAlAs/InP quantum dot infrared photodetector". *Appl. Phys. Lett.*, 90, 201109 (2007).

[127] S. Tsao, T. Yamanaka, S. Abdollahi Pour, et al. "Quantum dot in a well infrared photodetectors for high operating temperature focal plane arrays". *Proc. SPIE*, 7224, 72240V (2009).

[128] S. Slivken, C. Jelen, A. Rybaltowski, et al. "Gas-source molecular beam epitaxy growth of an 8.5 μm quantum cascade laser". *Appl. Phys. Lett*., 71, 2593-2595 (1997).

[129] N. Bandyopadhyay, Y. Bai, S. Tsao, et al. "Room temperature continuous wave operation of $\lambda \sim 3$-3.2 μm quantum cascade lasers". *Appl. Phys. Lett*., 101, 241110 (2012).

[130] S. Slivken, A. Evans, J. Nguyen, et al. "Overview of Quantum Cascade Laser Research at the Center for Quantum Devices". *Proc. SPIE*, 6900, 69000B (2008).

[131] Y. Bai, N. Bandyopadhyay, S. Tsao, et al. "Room temperature quantum cascade lasers with 27% wall plug efficiency". *Appl. Phys. Lett.*, 98, 181102 (2011).

[132] Y. Bai, S. Slivken, S. Kuboya, et al. "Quantum cascade lasers that emit more light than heat". *Nature Photonics*, 4, 99-102 (2010).

[133] D. Heydari, Y. Bai, N. Bandyopadhyay, et al. "High brightness angled cavity quantum cascade lasers". *Appl. Phys. Lett.*, 106, 091105 (2015).

[134] A. Evans and M. Razeghi. "Reliability of strain-balanced $Ga_{0.331}In_{0.669}As/Al_{0.659}In_{0.341}As$/InP quantum-cascade lasers under continuous-wave room-temperature operation". *Appl. Phys. Lett*., 88, 261106 (2006).

[135] Q. Y. Lu, Y. Bai, N. Bandyopadhyay, et al. "2.4 W room temperature continuous wave operation of distributed feedback quantum cascade lasers". *Appl. Phys. Lett.*, 98, 181106 (2011).

[136] B. Gokden, Y. Bai, N. Bandyopadhyay, et al. "Broad area photonic crystal distributed feedback quantum cascade lasers emitting 34 W at λ ~ 4.36 μm". *Appl. Phys. Lett*., 97, 131112 (2010).

[137] S. Slivken, N. Bandyopadhyay, S. Tsao, et al. "Sampled grating, distributed feedback quantum cascade lasers with broad tunability and continuous operation at room temperature". *Appl. Phys. Lett.*, 100, 261112 (2012).

[138] S. Slivken, N. Bandyopadhyay, Y. Bai, et al. "Extended electrical tuning of quantum cascade lasers with digital concatenated gratings". *Appl. Phys. Lett*., 103, 231110 (2013).

[139] S. Slivken, S. Sengupta and M. Razeghi. "High power continuous operation of a widely tunable quantum cascade laser with an integrated amplifier". *Appl. Phys. Lett.*, 107, 251101 (2015).

[140] N. Bandyopadhyay, M. Chen, S. Sengupta. "Ultra-broadband quantum cascade laser, tunable over 760 cm^{-1} with balanced gain". *Opt. Exp*., 23, 21159 (2015).

[141] W. Zhou, N. Bandyopadhyay, D. Wu, et al. "Monolithically, widely tunable quantum cascade lasers based on a heterogeneous active region design". *Sci. Rep.*, 6, 25213 (2016).

[142] S. Slivken, D. H. Wu and M. Razeghi. "Monolithic beam steering in a mid-infrared, surface-emitting, photonic integrated circuit". *Sci. Rep*. 7, 8472 (2017).

[143] Y. Bai, S. Tsao, N. Bandyopadhyay, et al. "High power, continuous wave, quantum cascade ring laser". *Appl. Phys. Lett.*, 99, 261104 (2011).

[144] D. H. Wu and M. Razeghi, "High power, low divergent, substrate emitting quantum cascade ring laser in continuous wave operation", APL Materials, 5, 035505, (2017).

[145] C. Sirtori, F. Capasso, J. Faist, et al. "Far-infrared generation by doubly resonant difference frequency mixingin a coupled quantum well two-dimensional electron gas system", Appl. Phys. Lett., 65, 445–447, (1994).

[146] Y. Bai, N. Bandyopadhyay, S. Tsao, et al. " Highly temperature insensitive quantum cascade lasers". *Appl. Phys. Lett.*, 97, 251104 (2010).

[147] N. Bandyopadhyay, Y. Bai, S. Slivken, et al. "High power operation of λ∼5.2–11 μm strain balanced quantum cascade lasers based on the same material composition". *Appl. Phys. Lett*., 105, 071106 (2014).

[148] M. A. Belkin, F. Capasso, F. Xie, et al. "Room temperature terahertz quantum cascade laser source based on intracavity difference-frequency generation". *Appl. Phys. Lett.*, 92, 201101 (2008).

[149] Q. Y. Lu, N. Bandyopadhyay, S. Slivken, et al. "Room temperature single-mode terahertz sources based on intracavity difference-frequency generation in quantum cascade lasers". *Appl. Phys. Lett*., 99, 131106 (2011).

[150] Y. Bai, S. Slivken, S. R. Darvish, et al. "Room temperature continuous wave operation of quantum cascade lasers with 12.5% wall plug efficiency". *Appl. Phys. Lett*., 93, 021103 (2008).

[151] A. Lyakh, R. Maulini, A. Tsekoun, et al. "3 W continuous-wave room temperature single-facet emission fromquantum cascade lasers based on nonresonant extraction design approach". *Appl. Phys. Lett*., 95, 141113 (2009).

[152] P. Q. Liu, A. J. Hoffman, M. D. Escarra, et al. "Highly power-efficient quantum cascade lasers". *Nature Photon.*, 4, 95 (2010).

[153] F. Xie, C. Caneau, H. P. Leblanc, et al. "Watt-level room temperature continuous-wave operation of quantum cascade lasers with λ >10 μm". *IEEE J. Sel. Topics Quantum Electron*., 19, 1200407 (2013).

[154] Q. Y. Lu, N. Bandyopadhyay, S. Slivken, et al. "Widely-tuned room temperature terahertz quantum cascade laser sources based on difference frequency generation". *Appl. Phys. Lett.*, 101, 251121 (2012).

[155] Q. Y. Lu, D. H. Wu, S. Sengupta, et al. "Room temperature continuous wave, monolithic tunable THz sources based on highly efficient mid-infrared quantum cascade lasers". *Sci. Rep*., 6, 23595 (2016).

[156] J. B. Khurgin, Y. Dikmelik, P. Q. Liu, et al. "Role of interface roughness in the transport and lasing characteristics of quantum-cascade lasers". *Appl. Phys. Lett*., 94, 091101 (2009).

[157] Q. Y. Lu, N. Bandyopadhyay, S. Slivken, et al. "Continuous operation of a monolithic semiconductor terahertz source at room temperature". *Appl. Phys. Lett*., 104, 221105 (2014).

[158] Q. Y. Lu, N. Bandyopadhyay, S. Slivken, et al. "High performance terahertz quantum cascade laser sources based on intracavity difference frequency generation". *Opt. Express*, 21, 968 (2013).

[159] P. K. Tien, R. Ulrich and R. J. Martin. "Optical second harmonic generation in form of coherent Cerenkov radiation from a thin-film waveguide". *Appl. Phys. Lett*., 17, 447 (1970).

[160] M. Theuer, G. Torosyan, C. Rau, et al. "Efficient generation of Cherenkov-type terahertz radiation from a Lithium Niobate crystal with a silicon prism output coupler". *Appl. Phys. Lett*. 88, 071122 (2006).

[161] K. Vijayraghavan, R. W. Adams, A. Vizbaras, et al. "Terahertz sources based on Čerenkov difference-frequency generation inquantum cascade lasers". *Appl. Phys. Lett.*, 100, 251104 (2012).

[162] Q. Y. Lu, N. Bandyopadhyay, S. Slivken, et al. "Room temperature terahertz quantum cascade laser sources with 215 μW output power through epilayer-down mounting". *Appl. Phys. Lett.*, 103, 011101 (2013).

[163] Q. Y. Lu and M. Razeghi. "Recent Advances in Room Temperature, High-Power Terahertz Quantum Cascade Laser Sources Based on Difference-Frequency Generation". *Photonics*, 3, 42 (2016).

[164] M. Razeghi, Q. Y. Lu, N. Bandyopadhyay, et al. "Recent development of high power, widely tunable THz quantum cascade laser sources based on difference-frequency generation". *Proc. SPIE*, 9585, 958502-1 (2015).

[165] Y. Jiang, K. Vijayraghavan, S. Jung, et al. "External cavity terahertz quantum cascade laser sources based on intra-cavity frequency mixing with 1.2–5.9 THz tuning range". *J. Opt.,* 16, 094002 (2014).

[166] Q. Y. Lu, S. Slivken, N. Bandyopadhyay, et al. "Widely tunable room temperature semiconductor terahertz source". *Appl. Phys. Lett*., 105, 201102 (2014).

[167] A. Hugi, G. Villares, S. Blaser, et al. "Mid-infrared frequency comb based on a quantum cascade laser". *Nature*, 492, 229 (2012).

[168] D. Burghoff, T. -Y. Kao, N. Han, et al. "Terahertz laser frequency combs". *Nat. Photonics,* 8, 462–467 (2014).

[169] Q. Y. Lu, M. Razeghi, S. Slivken, et al. "High power frequency comb based on mid-infrared quantum cascade laser at λ ~ 9 μm". *Appl. Phys. Lett.*, 106, 051105 (2015).

[170] M. Rösch, G. Scalari, M. Beck, et al. "Octave-spanning semiconductor laser". *Nat. Photonics*, 9, 42–47 (2015).

[171] G. Villares, A. Hugi, S. Blaser, et al. "Dual-comb spectroscopy based on quantum-cascade-laser frequency combs". *Nat. Commun.*, 5, 5192 (2014).

[172] Y. Yang, D. Burghoff, D. J. Hayton, et al. "Terahertz multi-heterodyne spectroscopy using laser frequency combs". *Optica*, 3, 499 (2016).

[173] Q. Y. Lu, D. H. Wu, S. Slivken, et al. "High efficiency quantum cascade laser frequency comb". *Sci. Rep*., 7, 43806 (2017).

[174] G. Villares, S. Riedi, J. Wolf, et al. "Dispersion engineering of quantum cascade laser frequency combs". *Optica*, 3, 252 (2016).

[175] Q. Y. Lu, S. Manna, S. Slivken, et al. "Dispersion compensated mid-infrared quantum cascade laser frequency comb with high power output". *AIP Advances*, 7, 045313 (2017).

[176] A. Tahraoui, S. Slivken, A. Matlis, et al. "High performance quantum cascade lasers (λ ~ 11 μm) operating at high temperature (T ≥ 425 K)". *Appl. Phys. Lett.*, 78, 416-418, (2001).

[177] J. S. Yu, S. Slivken, A. Evans, et al. "High-power continuous-wave operation of a 6 μm quantum-cascade laser at room temperature". *Appl. Phys. Lett.*, 83, 2503-2505 (2003).

[178] J. S. Yu, S. Slivken, S. R. Darvish, et al. "High-power, room-temperature and continuous-wave operation of distributed-feedback quantum-cascade lasers at λ ~ 4.8 μm". *Appl. Phys. Lett.*, 87, 041104 (2005).

[179] Y. Bai, S. R. Darvish, S. Slivken, et al. "Room temperature continuous wave operation of quantum cascade lasers with watt-level optical power". *Appl. Phys. Lett.*, 92, 101105 (2008).

[180] Y. Bai, S. Slivken, S. R. Darvish, et al. "High power broad area quantum cascade lasers". *Appl. Phys. Lett*., 95, 221104 (2009).